ADVANCED MATERIALS

Supporting Information

for *Adv. Mater.*, DOI 10.1002/adma.202303050

Enhanced Nitrate-to-Ammonia Efficiency over Linear Assemblies of Copper-Cobalt Nanophases Stabilized by Redox Polymers

*Wenhui He, Shubhadeep Chandra, Thomas Quast, Swapnil Varhade, Stefan Dieckhöfer, João R. C. Junqueira, Huimin Gao, Sabine Seisel and Wolfgang Schuhmann**

Supporting Information

Enhanced Nitrate-to-Ammonia Efficiency over Linear Assemblies of Copper-Cobalt Nanophases Stabilized by Redox Polymers

*Wenhui He, Shubhadeep Chandra, Thomas Quast, Swapnil Varhade, Stefan Dieckhöfer, João R. C. Junqueira, Huimin Gao, Sabine Seisel, and Wolfgang Schuhmann**

Experimental Section

1. Material synthesis.

1.1 Growth of ZIF-Co-80 nanosheets on Cu foil and carbon paper. Typically, a commercial Cu foil (2.5 × 0.5 cm^2, Sigma) or carbon paper (2.5 × 0.5 cm^2, Freudenberg) was immersed into a 12.5 mL growth solution, which was prepared by mixing 6 mL of $Co(NO_3)_2$ 6 H_2O aqueous solution (50 mM) with 6.5 mL of 2-methylimidazole aqueous solution (0.4 M). After being grown under static conditions at room temperature for 80 min, the purple ZIF-Co-80 films on Cu foil or carbon paper were taken out, washed with deionized water, and dried in a 70 ℃ oven. For uniform growth of ZIF-Co-80, the carbon paper was initially treated with 1 M HCl, washed with deionized water, then soaked in 2-methylimidazole solution (0.4 M) for 12 h, and dried by blotting paper before use.

1.2 EC-MOF for preparation of $CuCoS_x$ precursors on Cu foil. The $CuCoS_x$ precursors on Cu foil were synthesized by following an electrochemical conversion of metal-organic framework (EC-MOF) strategy.[1] Typically, the ZIF-Co-80 on Cu foil was converted into $CuCoS_x$ via continuous cyclic voltammetry (CV) scanning between −1.76 V and −0.28 V (vs. Ag/AgCl, *sat.* KCl) at a series of scan rates for different CV cycles (at 0.2 V s^{-1} for 1200 CV cycles, at 0.1 V s^{-1} for 300 CV cycles, at 0.05 V s^{-1} for 150 CV cycles and finally at 0.02 V s^{-1} for 100 CV cycles) in Ar-saturated electrolytes (aqueous solution of 0.5 M thiourea and 0.25 M KCl). The products (a black film) on Cu foil were rinsed with water and acetone, blow-dried by Ar gas and stored at -21 °C. Using the same procedures, CuS_x was prepared from Cu foil; the CoS_x nanosheets on carbon paper were synthesized using ZIF-Co-80 on carbon paper as precursors.

As a control, $Cu(OH)_2$ nanowires on Cu foil were synthesized by immersing a fresh Cu foil in a freshly mixing solution of NaOH (2.5 M) and $(NH_3)_2S_2O_8$ (0.125 M) with an equal volume in ice bath for 8 min. As for CoOHF nanowires on carbon paper,[2] a growth solution was prepared by dissolving $Co(NO_3)_2$ 6 H_2O (2 mmol), NH_4F (5 mmol), and urea (10 mmol) in 40 mL H_2O under vigorous stirring and then transferred into a Teflon-lined stainless autoclave (50 ml). After immersing a piece of HCl-treated carbon paper (2.3 × 6 cm^2), the growth solution was further sealed in the autoclave and maintained at 120 °C for 6 h in an oven. The pink products on carbon paper were washed with water and dried at room temperature.

1.3 Electrochemical redox-induced formation of $CuCoO_x$ nanoribbons. The linear assembly of Cu and Co nanophases on Cu foil was triggered by a continuous four-step galvanostatic electrolysis of $CuCoS_x$ on Cu foil for oxygen evolution in 0.1 M KOH, including 2.5 mA cm^2 for 2 h, 5 mA cm^2 for 2 h, 10 mA cm^2 for 3 h, and 20 mA cm^2 for 3h. The products ($CuCoS_x$-OER) were washed with water and acetone and then dried under Ar flow for further tests or characterizations. $CuCoO_x$ was prepared via LSV scanning activation of $CuCoS_x$-OER from 0.2 V to -0.35 V (vs. RHE) in 0.1 M KOH until the LSV curve achieved a steady state. As for $CuCoO_x$_40mA and $CuCoO_x$_80mA, the fourth step of galvanostatic electrolysis was fixed at 40 and 80 mA cm^{-2}, respectively.

As a control, H_2O_2-treated $CuCoS_x$ was prepared by immersing $CuCoS_x$ in 3 wt.% H_2O_2 ethanol solution for 12 hrs. For CuS_x, CoS_x, and H_2O_2-treated $CuCoS_x$ the same redox activation was implemented. LSV activation of $Cu(OH)_2$ nanowires produced CuO_x nanowires.

1.4 Preparation of viologen-based redox polymers (VRP)-protected $CuCoO_x$ ($CuCoO_x$_VRP). The synthesis of VRP is described in detail in supplemental note 1. To produce a uniform VRP gel protecting layer on $CuCoO_x$, poly(ethylene glycol)diglycidyl ether (PEGDGE 400) was used as crosslinkers of VRP. Typically, 2 μL of PEGDGE 400 was diluted in 98 μL water. Then, 3 μl aqueous solution of VRP (10 mg

ml^{-1}) was mixed with 1.5 µl of diluted PEGDGE 400. The mixed solution was dropped onto the $CuCoO_x$ surface and slowly dried at 4 °C overnight.

2. Material characterization.

SEM images were collected using a Quanta 3D FEG scanning electron microscope (FEI). TEM images, high-angle annular dark-field TEM images, SAED patterns, element mappings and EDX line scans were performed on a JEOL-2800 TEM/STEM system. XPS was carried out using an AXIS Nova spectrometer (Kratos Analytical) equipped with a monochromatic Al Kα X-ray source (1487 eV, 15 mA emission current). The binding energies of the core-level spectra were calibrated based on the C 1*s* signal located at 284.8 eV. The nuclear magnetic resonance (NMR) spectroscopy was recorded using a Bruker NMR spectrometer (400 MHz). XRD patterns were collected using a Bruker D_8 Discover X-ray diffractometer with Cu Kα radiation (λ = 1.5418 Å).

3. Electrochemical measurements and product analysis.

3.1 NO_3RR. All electrochemical measurements were performed using a three-electrode system connected to a Gamry interface 1000 workstation. Ag/AgCl (3 M KCl) and platinum mesh were used as the reference and counter electrodes, respectively. Electrode potentials were calibrated to the RHE reference scale using the equation $E_{RHE} = E_{Ag/AgCl} + 0.207\ V + 0.0591 \times pH$. The electrolyte was Ar-saturated 0.1 M KOH (pH 13) containing different concentrations of NO_3^-. The measurements were performed in an Ar-protected gas-tight H-type cell separated by a Nafion 117 membrane. The current density was normalized to the geometric electrode area. The voltage drop (iR_s) induced by the electrolyte resistance (R_s) was automatically compensated by the Gamry interface 1000 workstation. Potentiostatic electrolysis was carried out for 1 h in 30 mL cathode electrolyte with a stirring rate of 300 rpm, and then the electrolyte was stored at 4 °C before analysis. To assess the stability of catalysts, 4.5 hrs of continuous electrolysis were performed at -0.1 V (vs. RHE), during which the electrolytes (30 ml, 0.1 M KOH and 0.1 M nitrate) used in the cathodic compartment were pumped out and meanwhile fresh electrolytes were pumped in constantly at the rate of 1 mL min^{-1} (for retaining the concentration of NO_3^-). The C_{dl} was measured in Ar-saturated 0.1 M KOH by cyclic voltammetry (CV) in a non-faradaic potential range at different scan rates (20-100 mV s^{-1}). The plot of capacitive current differences anode and cathode [$(j_a - j_c)/2$] at a selected potential against the CV scan rates shows a linear relationship, and the slope is C_{dl}.

3.2 Determination of NH_3 and NO_2^-. The synthesized NH_3 was quantified using the indophenol blue method. Typically, a certain amount of post-electrolysis electrolytes was taken out and diluted to 2 ml. Then, 2 mL of 1 M KOH solution containing sodium citrate and salicylic acid (stored at 4 °C) was added, followed by adding 1 mL of freshly prepared 0.05 M $NaClO_4$. The mixed solution was further shaken for a few seconds. Finally, 0.2 mL of sodium nitroferricyanide solution (1 *wt.* %, stored at 4 °C) was added for the colour reaction. After 1 h at room temperature, the resulting solution was tested using an ultraviolet-visible (UV-vis) spectrophotometer. The absorption peak at ~655 nm was used to determine the concentration of NH_3. To quantify the amount of NH_3, a calibration curve was built using standard NH_4Cl (≥99.99 %) solution in 0.1 M KOH.

A specific colour reagent for NO_2^- quantification was prepared by dissolving 0.20 g of N-(1-naphthyl) ethylene diamine dihydrochloride and 4.0 g of sulfonamide in a mixed solution of 10 mL of phosphoric acid (85 wt. % in H_2O) (ρ = 1.7 g ml^{-1}) and 50 mL of deionized water. As for NO_2^- quantification, 5 mL of diluted post-electrolysis electrolyte was acidified by adding 1 mL HCl (1 M), and then 0.1 mL of colour reagent was added and shaken to obtain a uniform solution. After 20 min at room temperature, the UV-vis

absorbance of the solution at 540 nm was recorded. The amount of NO_2^- was measured using a calibration curve of $NaNO_2$ (≥96 %) solutions. Note that other probable products (e.g., N_2H_4 and NH_2OH) are ignored in our system because these products have high reactivity in basic media, which makes their concentrations to be very low and only measurable at intermediate times.

4. Calculation of the FE, Y_{NH3}, j_{NH3}, and EE_{NH3}.

4.1 Calculation of FE, Y_{NH3}, and j_{NH3}. The FE refers to the charge consumed for the formation of a specific product (NH_3 or NO_2^-) divided by the total charge passing through the electrodes (Q) during electrolysis. Given that the formation of one NH_3 molecule needs eight electrons, the FE of NH_3 (FE_{NH3}), Y_{NH3}, and j_{NH3} can be calculated as follows: $FE_{NH3} = (8 \times F \times C_{NH3} \times V)/Q$, $Y_{NH3} = (C_{NH3} \times V)/(A \times t)$, and $j_{NH3} = (Q \times FE_{NH3})/(A \times t)$, where F is the Faraday constant, C_{NH3} is the molar concentration of detected ammonia, V is the volume of the electrolytes, A is the electrode geometric area, and t is the reaction time. Given that two electrons are needed to produce one NO_2^- molecule, the FE of NO_2^- can be calculated as follows: $FE(NO_2^-) = (2 \times F \times C(NO_2^-) \times V)/Q$, where $C(NO_2^-)$ is the molar concentration of formed NO_2^-.

4.2 EE_{NH3} calculation. The half-cell energy efficiency of ammonia (EE_{NH3}) was defined as the ratio of fuel energy to applied electrical power, which was calculated with the following equation:

$$EE_{NH3} = \frac{(1.23 - E^0_{NH3})FE_{NH3}}{1.23 - E}$$

Where E^0_{NH3} is the equilibrium potential of nitrate electroreduction to ammonia (here it is calculated to be 0.6883 V vs. RHE in 0.1 M KOH and 10 mM nitrate), FE_{NH3} is the Faradaic efficiency for NH_3, E is the applied potential vs. RHE after iR_s correction. 1.23 V is the equilibrium potential of water oxidation, when assuming the overpotential of the water oxidation is zero.

Remarkably, E^0_{NH3} can be calculated from the corresponding theoretic equilibrium potential (E^0_0) when considering the impact of specific reaction conditions. According to the reaction equation of nitrate electroreduction to ammonia in alkaline conditions:

$$NO_3^- + 6H_2O + 8e^- \rightarrow NH_3 + 9OH^-$$

The theoretical equilibrium potential (E^0_0) of this reaction (vs. SHE) can be calculated based on the following equation:

$$E^0_0 = \frac{\sum \nu_1\mu_1 - \nu_2\mu_2}{23060n}$$

where ν_1 and ν_2 are the coefficient of reactants and products (e.g., the ν_1 of H_2O is 6, while the ν_2 of OH^- is 9), respectively. μ_1 and μ_2 are the energy of the reactant and product molecules, respectively (all energy values can be found in "*Atlas* of Electrochemical Equilibria in Aqueous Solutions"). The final value of E^0_0 for nitrate electroreduction to ammonia is calculated to be -0.1314 V (vs. SHE).

Moreover, based on the Nernst equation of the electroreduction of nitrate to ammonia the final E^0_{NH3} value is -0.0797 V (vs SHE) in 0.1 M KOH and 10 mM nitrate, which corresponds to 0.6883 V (vs RHE).

$$E^0_{NH3} = E^0_0 + \frac{0.0591}{n} ln \frac{[NO_3^-]}{[OH^-]^9}$$

where $[NO_3^-]$ is the concentration of nitrate (1-100 mM). $[OH^-]$ is the concentration of OH^- ions (0.1 M). n is the electron transfer number of the reaction (n = 8).

5. $^{14}NH_4^+$ and $^{15}NH_4^+$ quantification by ^1H NMR.

To quantify the yield of $^{14}NH_4^+$ (or $^{15}NH_4^+$) after electrolysis in 0.01 M $^{14}NH_4^+$ (or $^{15}NH_4^+$, >98 at.% ^{15}N) and 0.1 M KOH at 0.1 V (vs. RHE) for 1 h, a calibration curve based on ^1H NMR (400 MHz) measurements was firstly built using a series of $^{14}NH_4Cl$ (or $^{15}NH_4Cl$) standard solutions with defined concentrations (1, 2, 3, 4, and 5 mM). Typically, 125 μl of the standard solution or post-electrolysis electrolytes was mixed with 125 μl of 10 mM maleic acid in DMSO-D_6 (99.9 atom % D), 50 μl of 4 M H_2SO_4 in DMSO-D_6, and 750 μl of DMSO-D_6. The mixed solutions were transferred into NMR tubes and tested under a mode of water peak suppression. The tested ^1H NMR peak area integral ratio of $^{14}NH_4^+$ (or $^{15}NH_4^+$) to maleic acid is positively correlated with the concentrations of $^{14}NH_4^+$ (or $^{15}NH_4^+$).

6. *In-situ* Raman spectroscopy.

Raman spectroscopy was recorded using a Lab-RAM HR Raman microscopy system (Horiba Jobin Yvon, HR550) equipped with a 532 nm laser as the excitation source, a water immersion objective (Olympus LUMFL, 60×, numerical aperture = 1.0), a monochromator (1800 grooves/mm grating), and a Synapse CCD detector. Each spectrum is an average of two to five continuously acquired spectra with a collection time of 50 s each. As for the in-situ Raman tests, a three-electrode electrochemical cell was employed, where Pt wires and Ag/AgCl (3M KCl) were used as counter and reference electrodes, respectively. In order to alleviate the etching of the objective lens in 0.1 M KOH electrolyte, 0.01 M KOH (pH 12) was used instead. K_2SO_4 (≥99.0 %) was added to ensure sufficient ionic conductivity of the electrolytes and provides SO_4^{2-} ions as an external Raman reference (~982 cm^{-1}). Typically, when there is 0.01 M KNO_3 (or 0.1 M KNO_3), the supporting electrolytes were 0.01 M KOH and 0.04 M K_2SO_4. Otherwise, the electrolytes were 0.01 M KOH and 0.045 M K_2SO_4.

Supplementary Notes

Supplementary Note 1. Density functional theory (DFT) calculations.

DFT calculations were performed with a periodic slab model using the Vienna Ab initio Simulation Package (VASP) code.[3] Generalized gradient approximation (GGA) with the exchange-correlation functional in the Perdew-Burke-Ernzerhof (PBE) form was adopted.[4] The projector-augmented wave (PAW) pseudopotentials were utilized to deal with the electron-ion interactions, and the cut-off energy for the plane-wave basis was set as 400 eV.[5] DFT+U method was used to better describe the on-site coulomb (U) correlation of the localized 3d electrons for transition metal Co with U - J = 3.3 eV and Cu with U - J = 4.0 eV.[6] The 5×5 Cu (111), 5×5 Cu (100), 4×3 CuO (100), 2×2 Cu_2O (111), and 4×4 CoO (111) surface slabs were constructed with four layers to ensure the large lateral lattice (1.2 ~ 1.6 nm). We used the model that a Co_3O_3 cluster deposited on a four-layer Cu (100) slab to stimulate the Cu-CoO interface. Similarly, Cu-Cu_2O, CuO-Cu_2O, CuO-CoO, Cu_2O-CoO interfaces were simulated by Cu_2O (111) / Cu_4, Cu_2O (111) / Cu_3O_3, CuO (100) / Co_3O_3 , Cu_2O (111) / Co_3O_3, respectively. A vacuum layer of 15 Å was inserted along the z direction (perpendicular to the surface slab) to avoid periodic image interactions. During the structural optimization, the bottom two atomic layers of all surface slabs were fixed while other layers and adsorbates were fully relaxed. A k-mesh of 2×2×1 was sampled for the Brillouin zone. Grimme's semiempirical DFT-D3 scheme of dispersion correction was adopted to describe the van der Waals (vdW) interactions. Dipole corrections were used to minimize inaccuracies in the total energy because of simulated slab interactions.[7] The convergence criteria for the electronic self-consistent loop and the Hellmann-Feynman forces on each atom were taken to be 10^{-5} eV and 0.02 eV $Å^{-1}$, respectively. The adsorption energy (E_{ads}) for the species in the NRA process is calculated as follows:

$$E_{ads} = E_{adsorbate+slab} - E_{slab} - E_{adsorbate},$$

where $E_{adsorbate+slab}$, E_{slab} and $E_{adsorbate}$ are the total energies of the slab together with adsorbates, clean slab and free adsorbate, respectively.

Supplementary Note 2. Synthesis of viologen-based redox polymers.

Materials: All chemicals and material were purchased from Sigma-Aldrich, Alfa Aesar, Acros Organics, VWR, Fisher Chemicals or Merck, and they were used as received except otherwise noted. Dry solvents were purchased from Acros Organics (extra dry and stored over molecular sieves, AcroSeal bottles). Deuterated solvents were stored at 4 °C, and DMSO-d_6 was stored at room temperature. All reactions and manipulations were conducted using standard Schlenk technique under argon atmosphere.

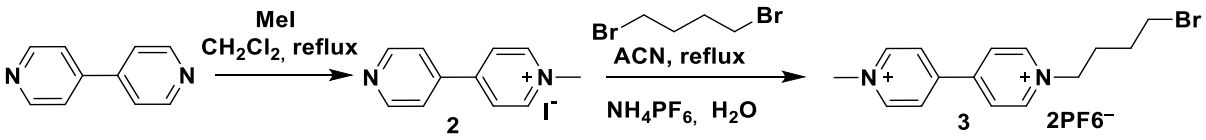

The monomethylated compound **2** was synthesized according to a procedure reported.[8] The monomethylated compound **2** (100 mg, 0.33 mmol) was dissolved in around 10 mL of dry ACN. Then, dibromo butane (106 mg, 0.495 mmol, 1.5 equivalent) were added and the reaction mixture was heated to 90 °C and stirred overnight. The red slurry was cooled down to room temperature, the precipitate was filtered off and washed with 150 mL of EtOAc. For the metathesis reaction of the bromo-iodo compound with PF_6^-, the red powder was dissolved in water (≈30 mL) and 6 mL of an aqueous NH_4PF_6 (1 M) were added. The mixture was thoroughly stirred and then cooled to 4 °C to complete the precipitation of the colorless PF_6^- salt. The precipitate was filtered off and washed with 20 mL of cold water. Finally, the product (compound **3**) was dried under reduced pressure to receive a slightly brownish powder.

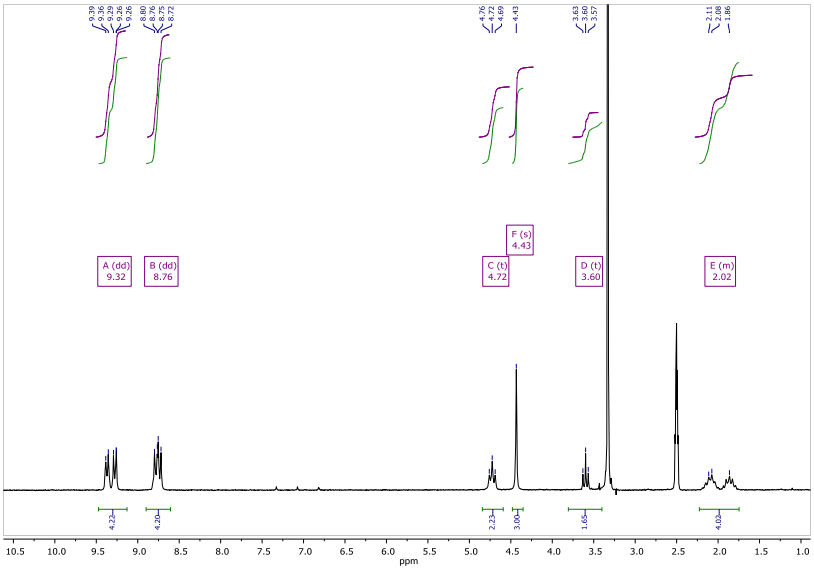

Figure S1. The 1H NMR spectrum of Compound 3. ^{1}H NMR (200 MHz, DMSO-d_6) δ 9.32 (dd, *J* = 18.9, 6.3 Hz, 4H), 8.76 (dd, *J* = 8.9, 6.7 Hz, 4H), 4.72 (t, *J* = 7.1 Hz, 2H), 4.43 (s, 3H), 3.60 (t, *J* = 6.5 Hz, 2H), 2.27 – 1.59 (m, 4H).

Synthesis of the Polyvinyl pyridine (PVP)-Viologen Redox Polymer

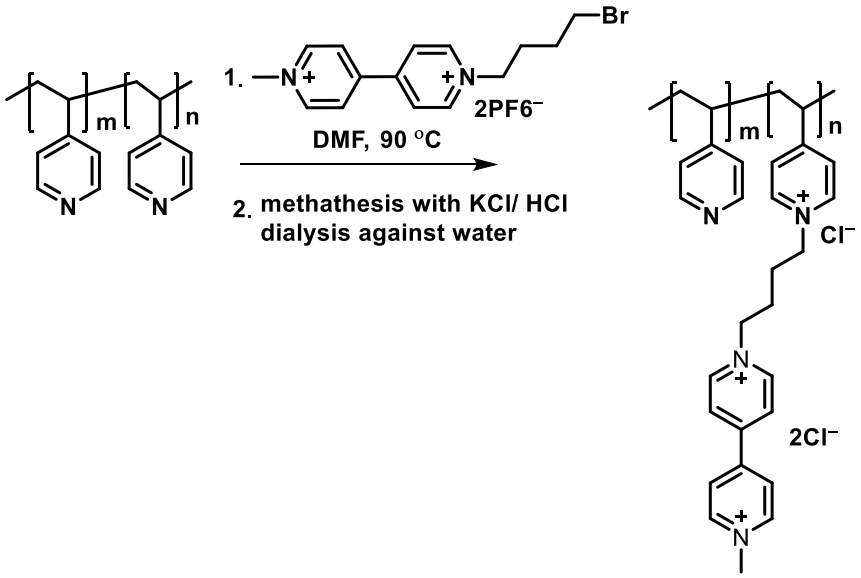

The polymer was synthesized according to a procedure described previously.[9] Polyvinyl pyridine (21 mg, 0.20 mmol) and compound **3** (143 mg, 0.24 mmol) was dissolved in DMF and heated at 90 °C for 24 hrs. After cooling down to room temperature, 60 mL of EtOAc were added. The precipitate was separated by centrifugation (4000 rpm, 8 min) and washed with 70 mL of EtOAc. The solid was again separated by centrifugation (4000 rpm, 10 min). The clear and colorless solution was discarded, and the solid material was dried in air. The crude product (145 mg) was suspended in water and dissolved by adding diluted HCl solution (total volume 23 ml). The use of HCl ensures the exchange of the bromide and iodide counter ions against chloride ions and meanwhile the increased solubility in water due to partial protonation of the pyridine cores. The polymer was purified by ultracentrifugation and then washed with KCl aqueous solution (0.1 M) and deionized water using membrane filters with a molecular weight cut-off of 5 kDa (Vivaspin 500, Sartorius).

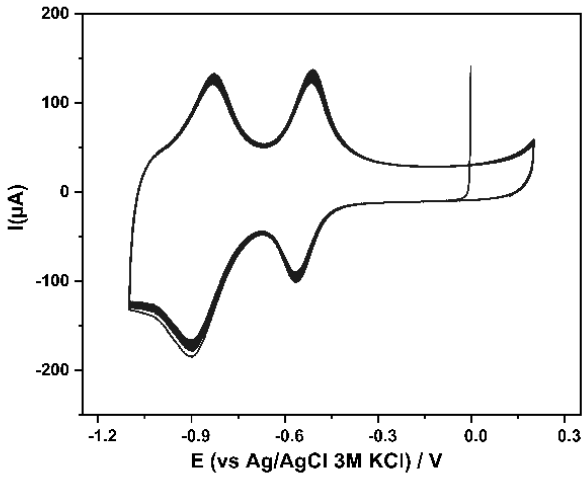

Figure S2. Cyclic voltammetry of the viologen-based redox polymer (VRP) in 0.1 M KOH solutions. The redox potentials of the first and second reduction process of polymers were estimated from cyclic voltammetric experiments in 0.1 M KOH solutions at a glassy carbon electrode.

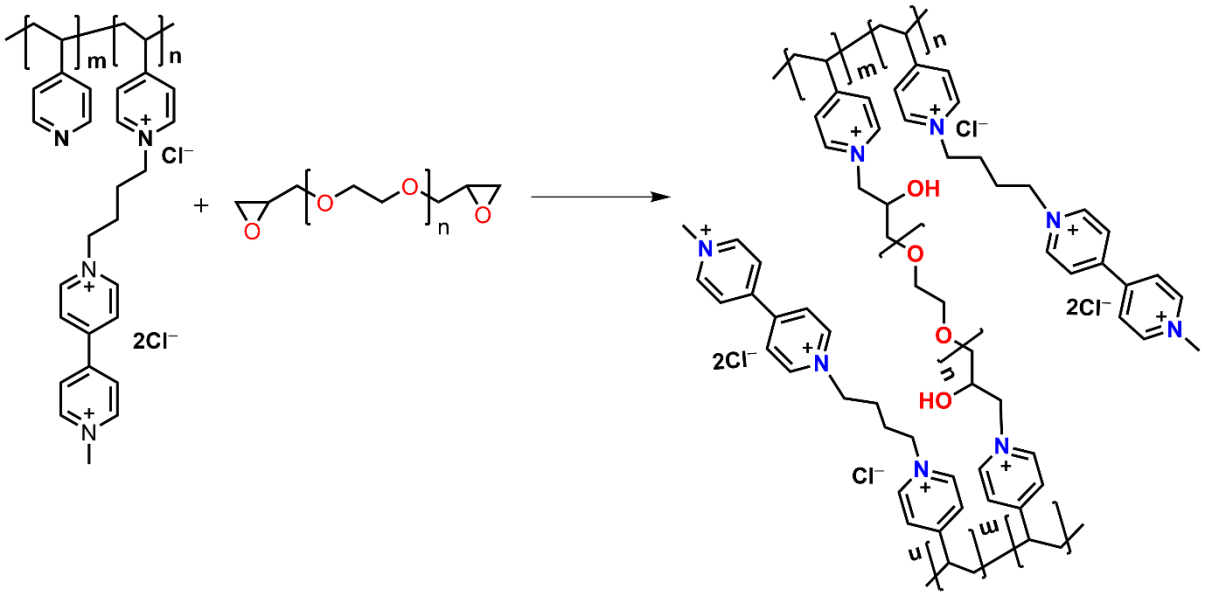

Figure S3. **Preparation of VRP hydrogel.** Schematic illustration of a crosslinked reaction between viologen-based redox polymers (VRP) and organic linkers (poly(ethylene glycol)diglycidyl ether, PEGDGE400). An appropriate amount of mixed aqueous solution of VRP and PEGDGE400 (mass ratio 10: 1) was applied dropwise onto the $CuCoO_x$, giving a loading mass of VRP to be 0.1 mg cm^{-2} after dried at 4℃ overnight.

Supplementary Figures

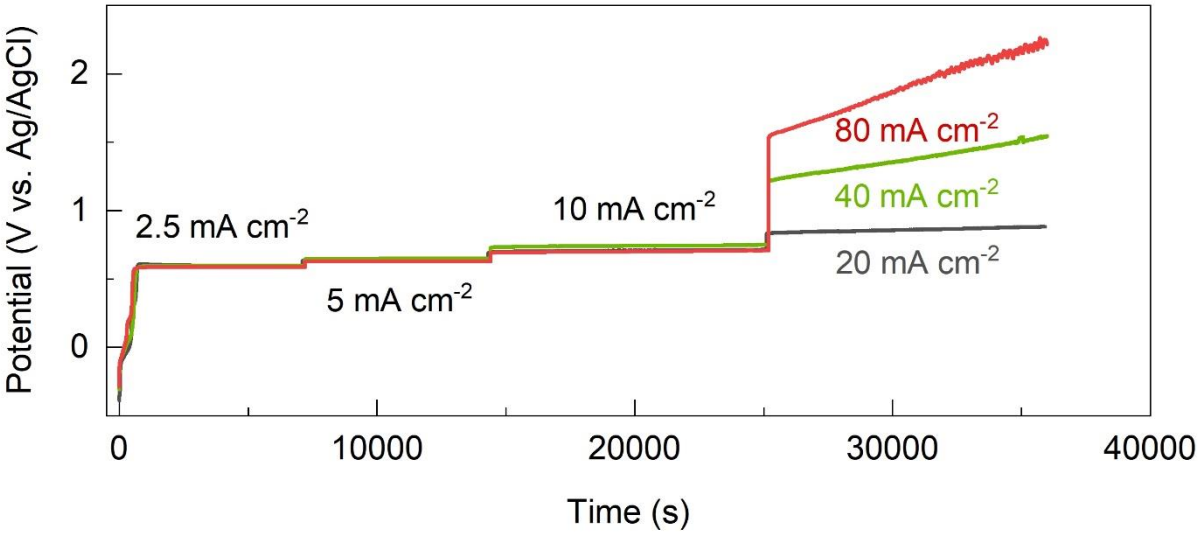

Figure S4. Galvanostatic electrolysis for linearly assembling Cu-Co nanophases. Electrochemical oxidation-induced conversion of $CuCoS_x$ nanosheets into $CuCoS_x$-OER nanoribbon arrays via four-step continuous galvanostatic electrolysis for oxygen evolution reaction (OER) in 0.1 M KOH. The current densities at each step are marked and the three types of products after activation were named as $CuCoO_x$ (20 mA cm^{-2}), $CuCoO_x$_40mA (40 mA cm^{-2}), and $CuCoO_x$_80mA (80 mA cm^{-2}), respectively, based on the fourth-step current densities.

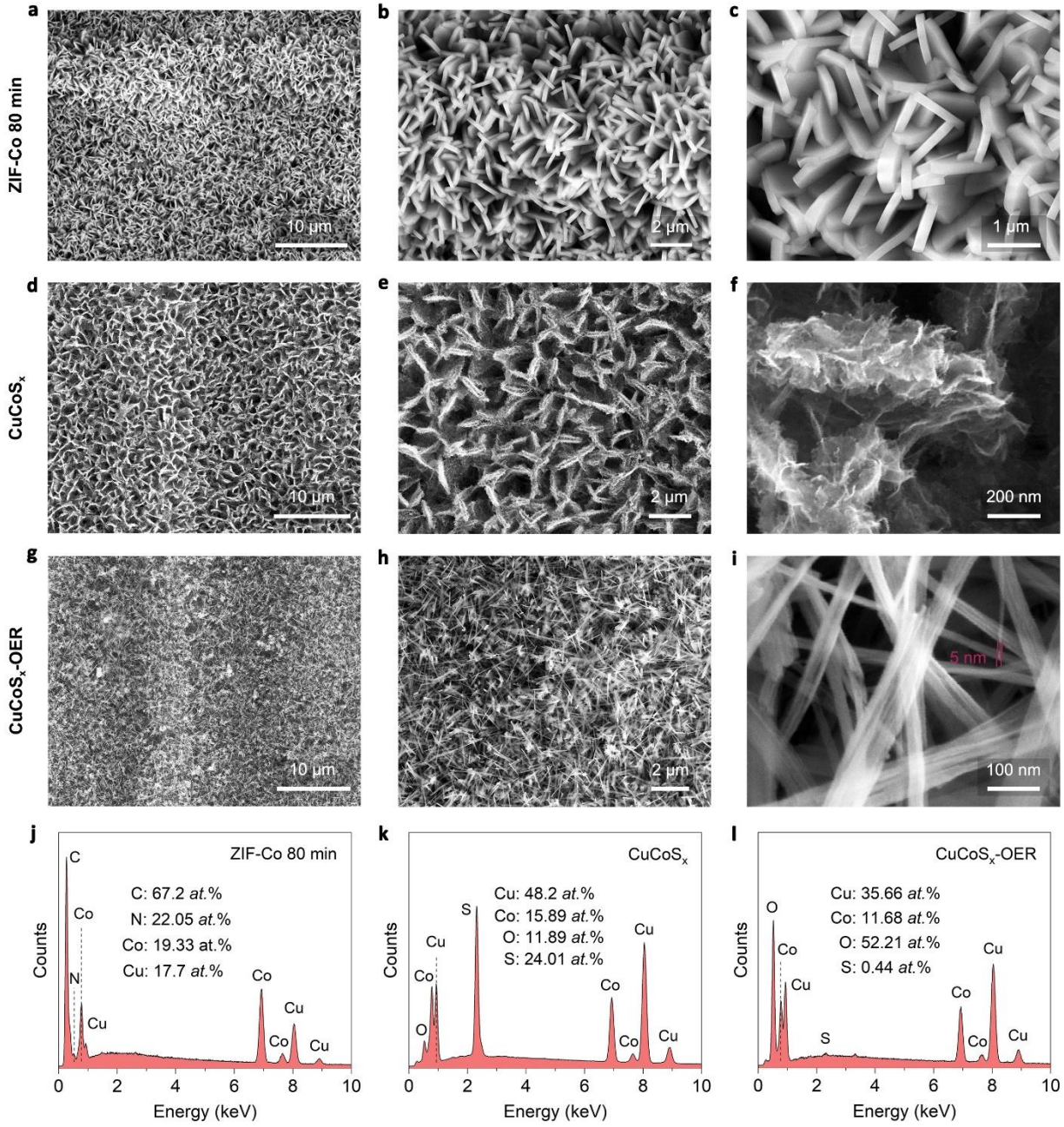

Figure S5. Morphology and composition of ZIF-Co 80 min, $CuCoS_x$ and $CuCoS_x$-OER. (**a−c**) SEM images of ZIF−Co (80 min) nanosheets grown on Cu foil with different magnification. (**d−f**) SEM images of $CuCoS_x$ synthesized by electrochemical conversion of ZIF−Co (80 min). (**g−i**) SEM images of $CuCoS_x$-OER obtained from a four-step continuous electrochemical oxidation of $CuCoS_x$. (**j−l**) The corresponding energy dispersive X−ray spectroscopy (EDS) of ZIF−Co 80 min (**j**), $CuCoS_x$ (**k**), and $CuCoS_x$-OER (**l**).

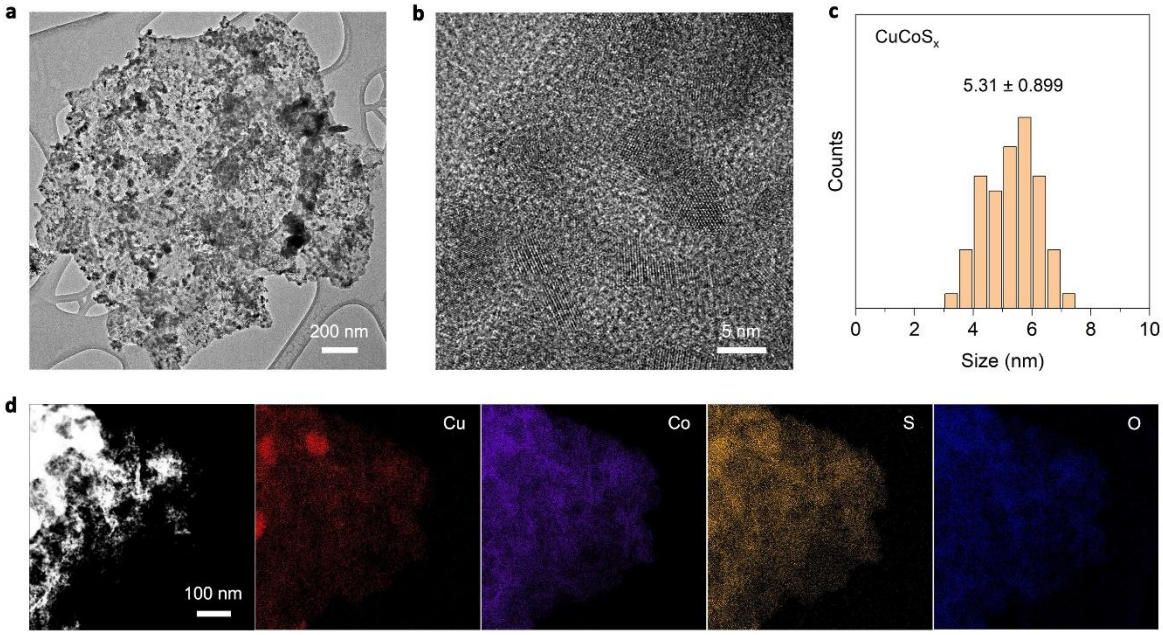

Figure S6. Nanostructure and element distribution of $CuCoS_x$. (**a-b**) Typical TEM and HR−TEM images of $CuCoS_x$ nanosheets. (**c**) The size distribution of nanocrystals in $CuCoS_x$, showing a mean size of 5.31 ± 0.899 nm. (**d**) High-angle annular dark-field (HAADF) TEM and EDX mapping of $CuCoS_x$ nanosheets.

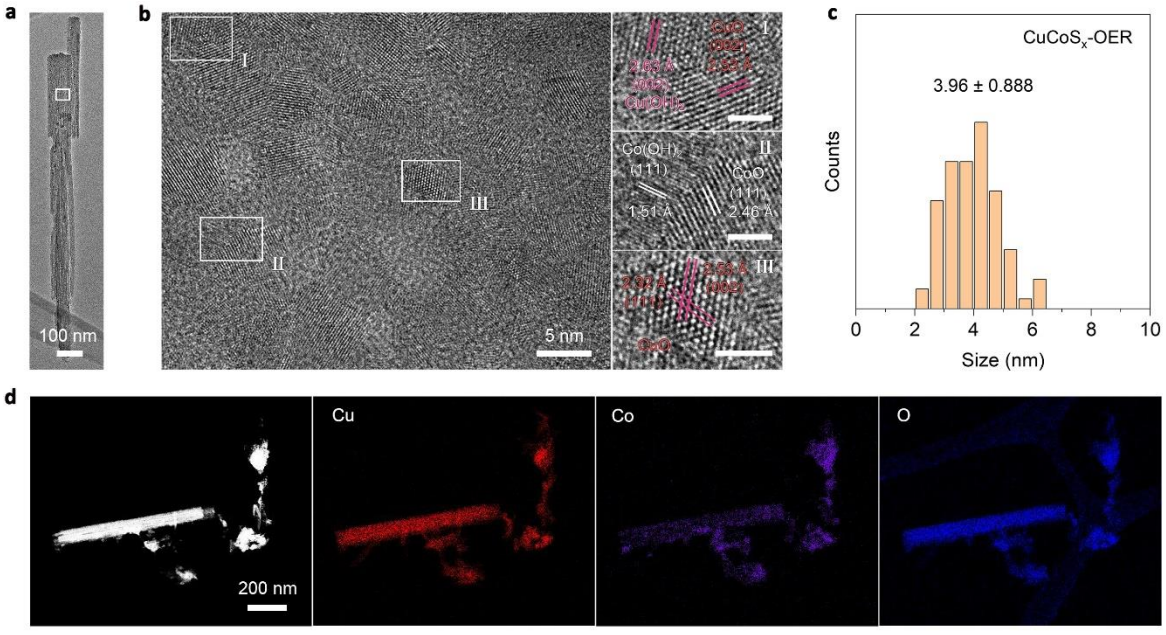

Figure S7. Nanostructure and element distribution of $CuCoS_x$-OER. (**a-b**) Typical TEM and HR−TEM images of $CuCoS_x$-OER nanoribbons. The crystalline lattices in three selected regions (I, II, and III) in (**b**) reveal the coexistence of $Cu(OH)_2$, CuO, $Co(OH)_2$, and CoO nanocrystals. (**c**) The size distribution of nanocrystals in $CuCoS_x$-OER, showing a mean size of 3.96 ± 0.888 nm. (**d**) High-angle annular dark-field (HAADF) TEM and EDX mapping of $CuCoS_x$-OER nanosheets.

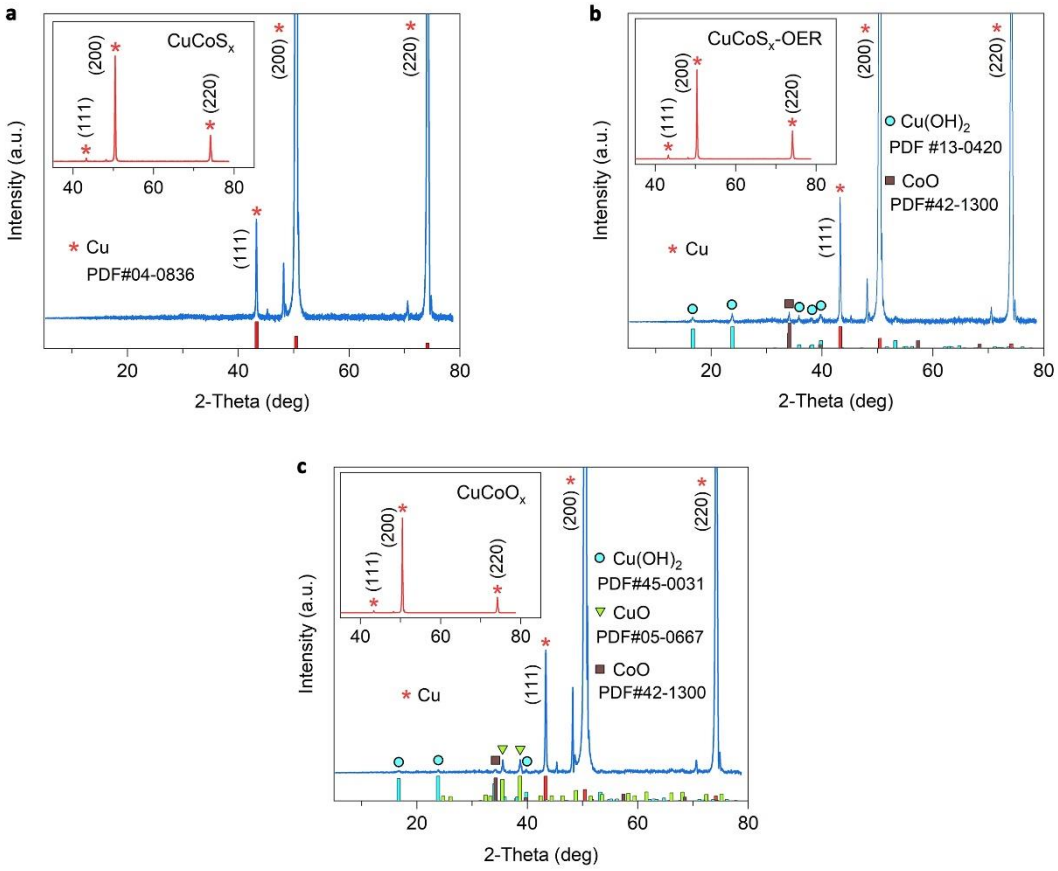

Figure S8. X−ray diffraction (XRD) patterns of the samples. (**a**) $CuCoS_x$. (**b**) $CuCoS_x$-OER. (**c**) $CuCoO_x$. All the samples on Cu foils show preferential exposure of the Cu (200) facet.

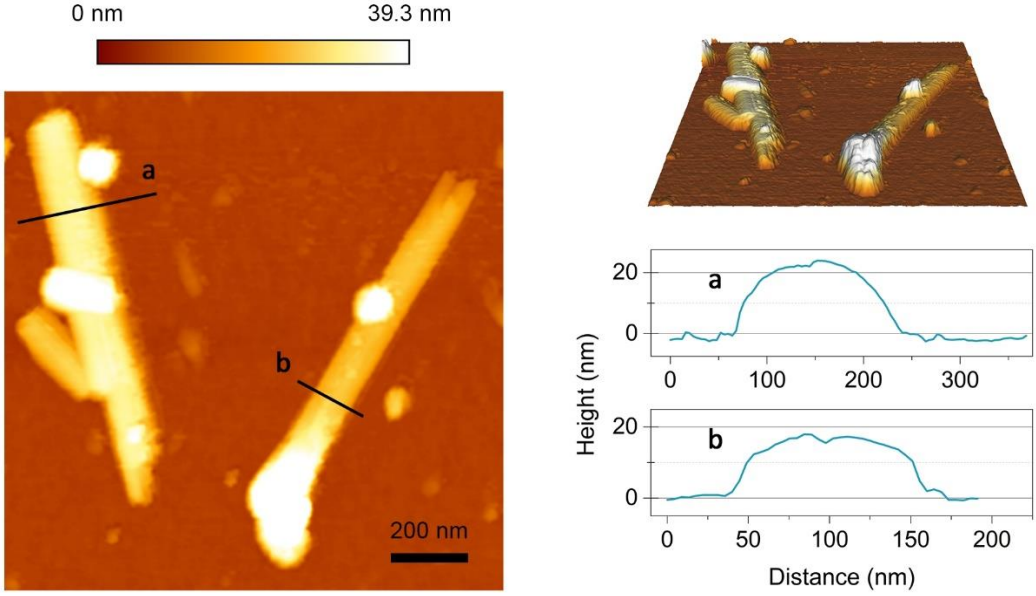

Figure S9. Microscopy and thickness of $CuCoO_x$ nanoribbons. A typical AFM image of $CuCoO_x$ deposited on SiO_2/Si substrate and the corresponding 3D profile image, showing that the thickness of $CuCoO_x$ is about 20 nm.

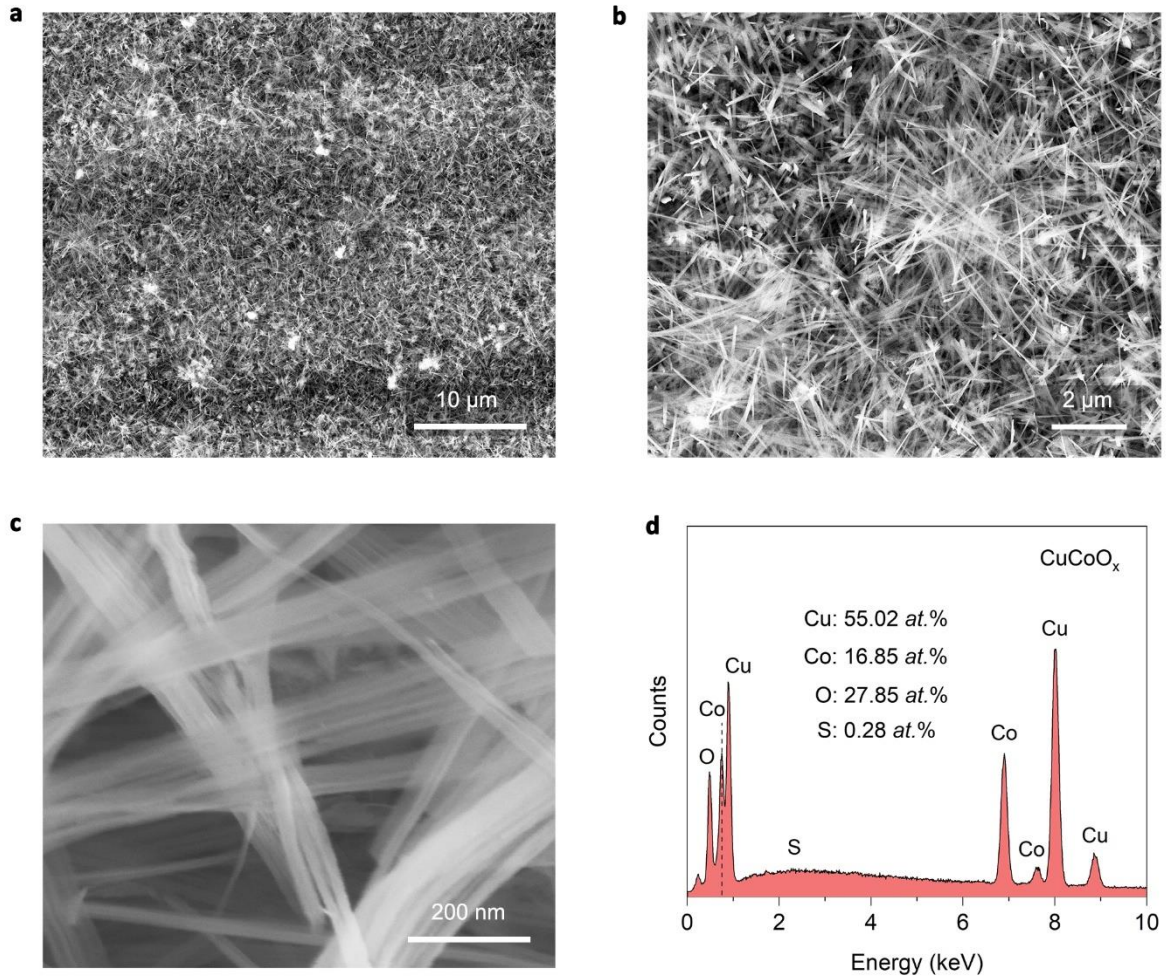

Figure S10. Morphology and composition of $CuCoO_x$. (**a−c**) Typical SEM images of $CuCoO_x$ on Cu foil with different magnifications. (**d**) EDS spectra of $CuCoO_x$.

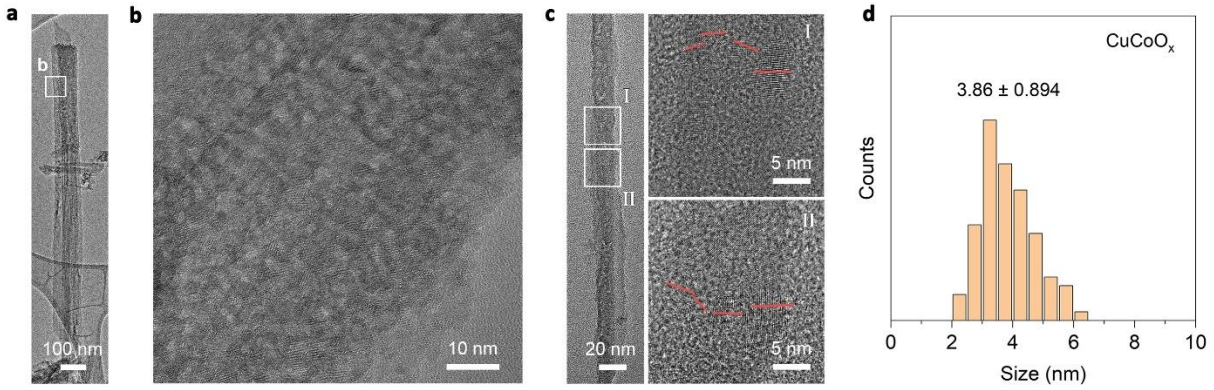

Figure S11. Nanostructure of $CuCoO_x$. (**a-c**) Typical TEM and HR−TEM images of $CuCoO_x$ nanoribbons with different widths. The HR-TEM images of two selected regions (I and II) in (**c**) reveal that the nanoribbons with a width of ~17 nm is assembled by four nanocrystals with a size of 2-6 nm. (**d**) The size distribution of nanocrystals in $CuCoO_x$, showing a mean size of 3.86 ± 0.894 nm.

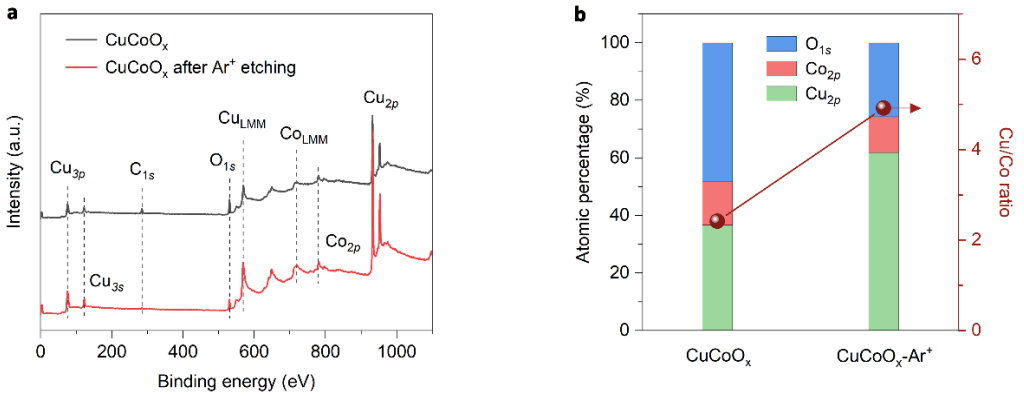

Figure S12. X−ray photoelectron spectroscopies (XPS) of $CuCoO_x$. (**a**) XPS survey spectra of $CuCoO_x$ before and after Ar^+ etching for 60 s. (**b**) XPS−determined atomic percentages and Cu/Co atomic ratios of $CuCoO_x$.

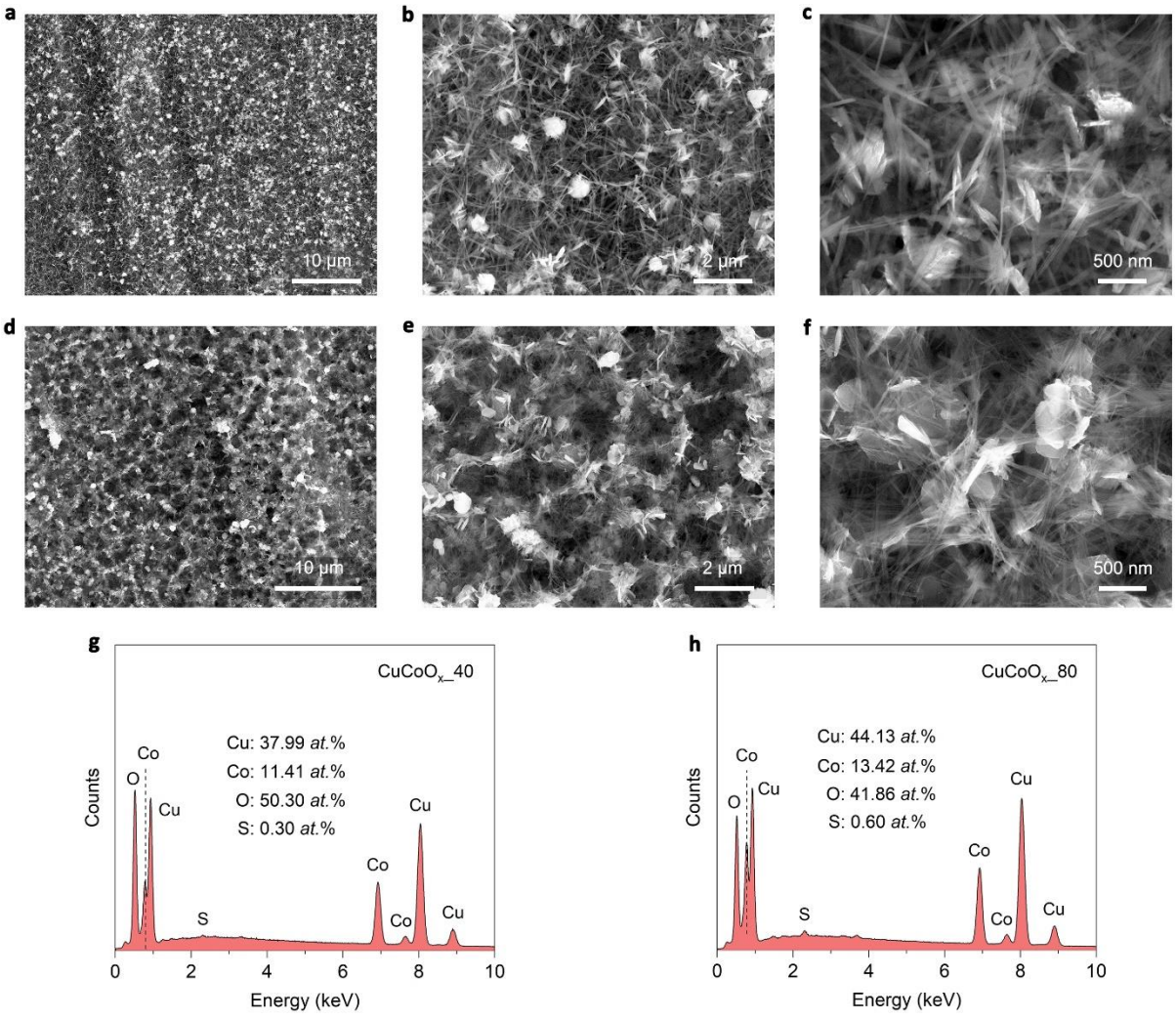

Figure S13. Morphology and composition of $CuCoO_x$_40mA and $CuCoO_x$_80mA. (**a**−**c**) SEM images of $CuCoO_x$_40mA on Cu foil with different magnifications. (**d**−**f**) SEM images of $CuCoO_x$-80mA with different magnifications. The corresponding EDS spectra of $CuCoO_x$_40mA (**g**) and $CuCoO_x$-80mA (**h**).

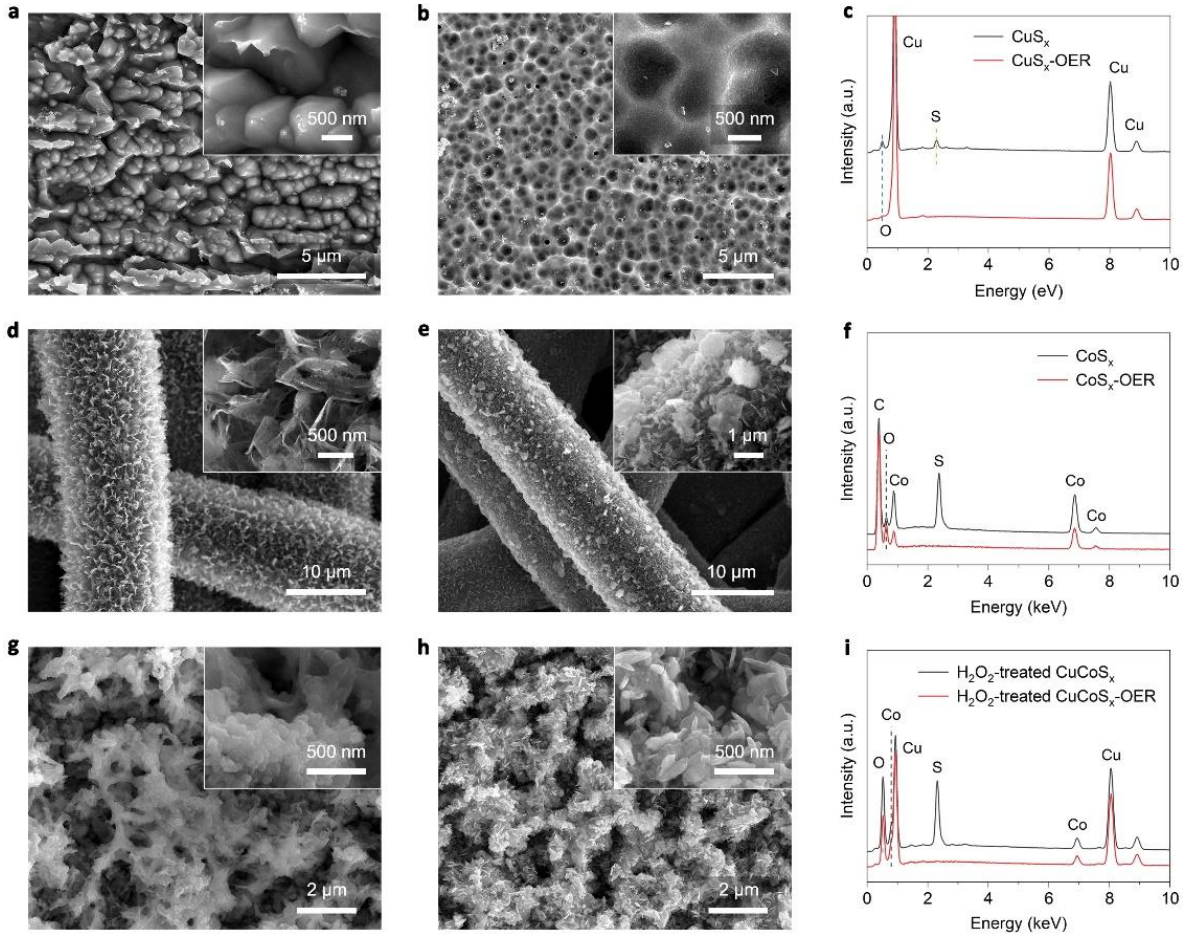

Figure S14. Morphology and composition of CuS_x, CoS_x and H_2O_2-treated $CuCoS_x$ before and after procedural four-step oxidation activation. (**a**−**c**) Typical SEM images of CuS_x on Cu foil (**a**), CuS_x-OER (**b**), and EDX spectra (**c**). (**d**−**f**) Typical SEM images of CoS_x on carbon papers (**d**), CoS_x-OER (**e**), and EDX spectra (**f**). (**g**−**i**) Typical SEM images of H_2O_2-treated $CuCoS_x$ on Cu foil (**g**), H_2O_2-treated $CuCoS_x$-OER (**h**), and EDX spectra (**i**). The insets show the corresponding SEM images with higher magnification.

Key influencing factors of electrochemical redox-induced $CuCoO_x$ nanoribbon formation

To identify the impact of different constituting elements on the structural transformation, we synthesized control samples of CuS_x and CoS_x using the same electrochemical method and we also prepared a H_2O_2-treated $CuCoS_x$ sample (please see details in the experimental section). As for CuS_x, there is no nanosheet formation in absence of Co (Figure S14a). After the OER activation, the island-like surface of CuS_x was etched to many pits (Figure S14b). CoS_x showed a nanosheet morphology (Figure S14d), indicating that the initial nanosheet morphology of $CuCoS_x$ is derived from the cobalt-based sulfide. After OER activation, the CoS_x nanosheets were then converted into hexagonal $Co(OH)_2$ nanosheets without forming nanoribbons (Figure S14e). Additionally, to identify the role of S, we used H_2O_2 to partially oxidize $CuCoS_x$. H_2O_2-treated $CuCoS_x$ showed a reticular structure, which was completely converted into nanosheets after OER activation, even if both Cu and Co were present (Figure S14g-i). These results suggest that the OER-induced conversion of $CuCoS_x$ nanosheets into $CuCoO_x$ nanoribbons is due to the coexistence of Cu, Co, and S. According to our previous report, the CoS_x phase is more easily oxidized than the CuS_x phase[11]. We suppose that the sequential oxidation of sub-5 nm CoS_x phases and then of the CuS_x phases are essential for forming nanoribbon structures during the OER activation process. When the sub-5 nm CoS_x

phases were initially oxidized to OER-active CoO_x phases, releasing of SO_4^{2-} and O_2 may promote the separation of the formed sub-5 nm CoO_x nanocrystals. At the same time, the CuS_x phases adjacent to the CoO_x could play the role of electron transfer nodes, owing to their higher conductivity, which contributes to the formation of nanowires (Figure S5i). The ultrathin nanowires further assemble under formation of nanoribbons, as evidenced by the beam-like structure assembled from many monofilaments (Figure S5i and S10c). Finally, the formed CoO_x phases would be exposed on the surface of nanoribbons for driving the OER, while the skeleton of the nanoribbons is composed of the more conductive Cu-based phases. This is supported by the Ar^+-etching XPS tests (Figure S12).

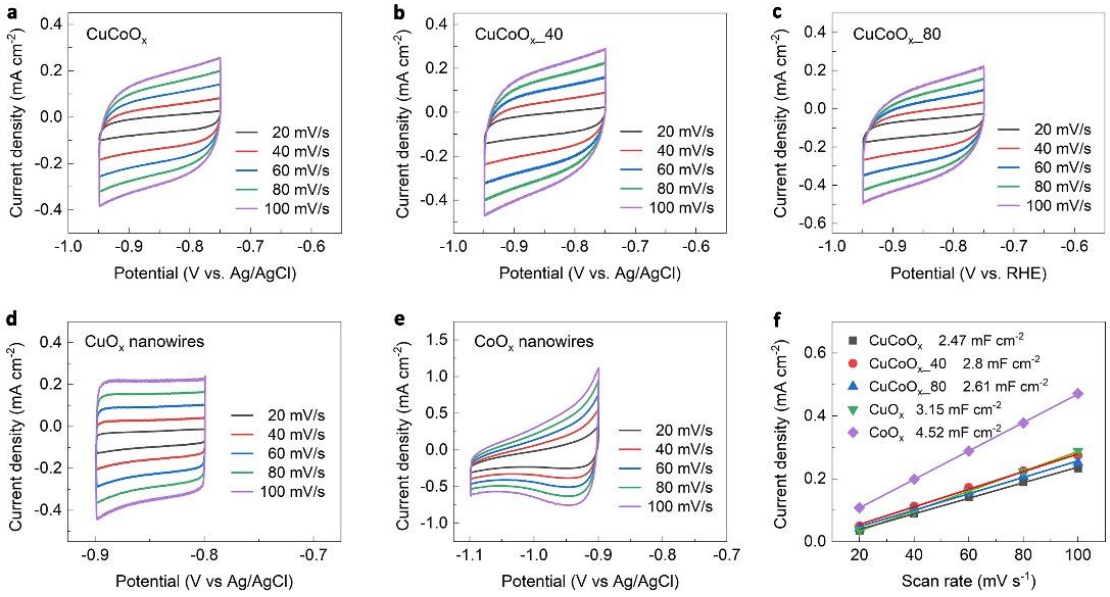

Figure S15. Cyclic voltammograms (CV) for the determination of the double−layer capacitance of different samples in Ar−saturated 0.1 M KOH. (**a**) $CuCoO_x$. (**b**) $CuCoO_x$_40mA. (**c**) $CuCoO_x$_80mA. (**d**) pure CuO_x nanowire. (**e**) pure CoO_x nanowires. (**f**) Plots of the current densities against CV scan rates. The slopes are positively correlated with the electrochemical double−layer capacitance per geometric area of the electrode and show also a correlation to the electrochemical surface area (ECSA).

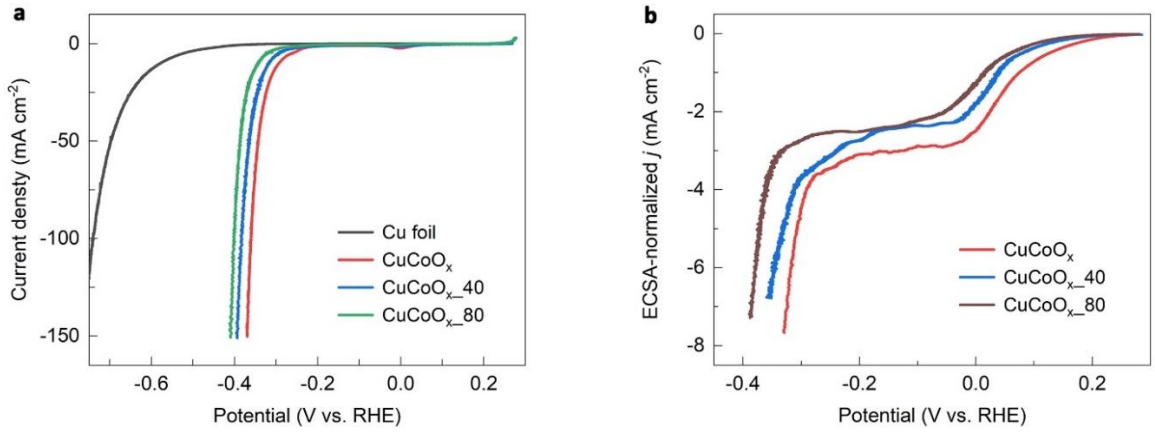

Figure S16. Linear sweep voltammograms (LSV) of $CuCoO_x$, $CuCoO_x$_40mA and $CuCoO_x$_80mA. (**a**) The LSVs of the samples in 0.1 M KOH electrolytes, showing the H_2−evolving activities (HER) of the catalysts. (**b**) ECSA-normalized LSV curves of $CuCoS_x$, $CuCoO_x$_40mA, and $CuCoO_x$_80mA in 0.1 M KOH and 0.01 M NO_3^-. The ECSA of the catalysts is listed in **Table S3**. The LSVs were recorded at a scan rate of 5 mV s^{-1}.

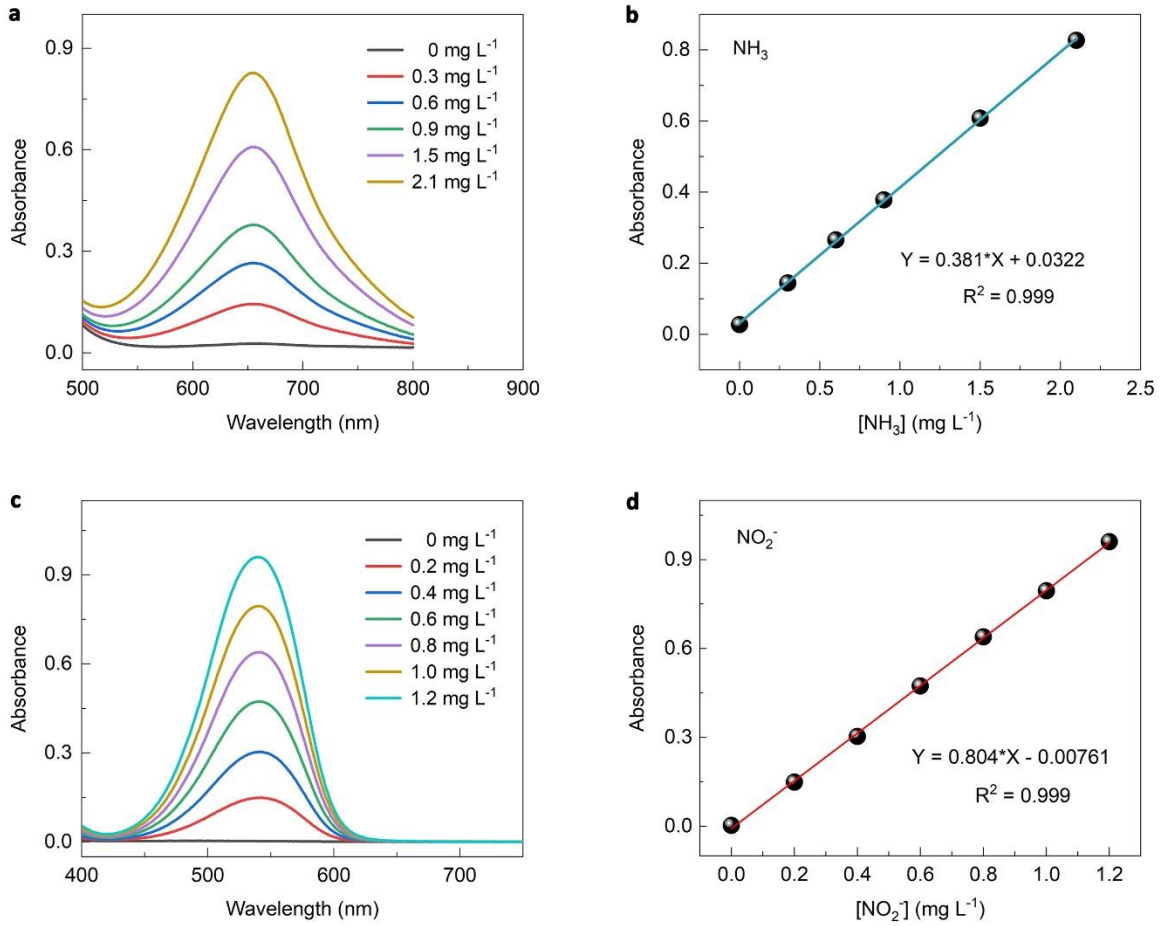

Figure S17. NH_3 and NO_2^- quantification using UV−vis absorption spectroscopy. (**a**, **b**) UV−vis absorption spectra and corresponding calibration curve for the NH_3 assay using the indophenol blue method. (**c**, **d**) UV−vis adsorption spectra and corresponding calibration curve for the NO_2^- assay.

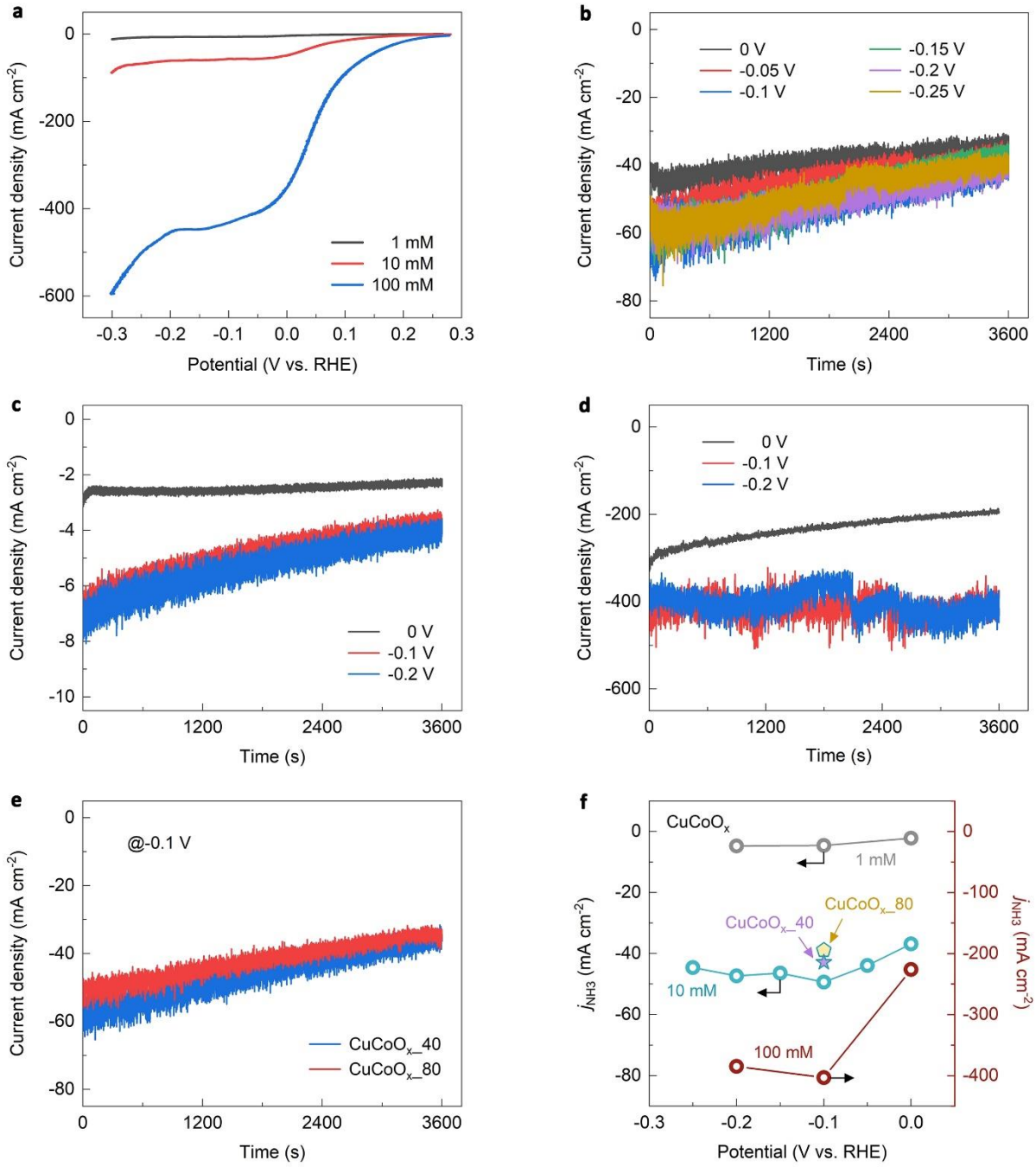

Figure S18. NO_3^- reduction activity of $CuCoO_x$, $CuCoO_x$_40mA and $CuCoO_x$_80mA. (**a**) LSV curves of $CuCoO_x$ in 0.1 M KOH with 1, 10, and 100 mM NO_3^-. (**b-c**) Chronoamperometry curves of $CuCoO_x$ at different potentials for 1 h in 0.1 M KOH with 10 mM NO_3^- (**b**), 1 mM NO_3^- (**c**), and 100 mM NO_3^- (**d**). (**e**) Chronoamperometry curves of $CuCoO_x$_40mA and $CuCoO_x$_80mA at -0.1 V (vs. RHE) for 1 h in 0.1 M KOH and 10 mM NO_3^-. (**f**) Partial current densities of NH_3 (j_{NH3}) on $CuCoO_x$ in 1, 10, and 100 mM nitrate, as well as j_{NH3} on $CuCoO_x$_40mA and $CuCoO_x$_80mA in 10 mM nitrate. The LSVs in (**a**) were recorded at a scan rate of 5 mV s^{-1}.

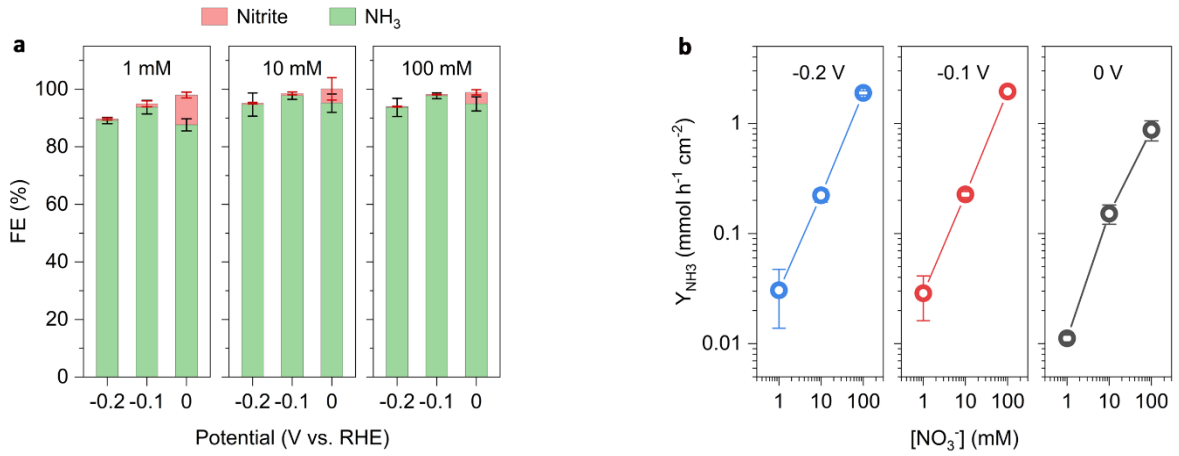

Figure S19. NH_3 synthesis performance of $CuCoO_x$ in different concentrations of NO_3^-. (**a**) FE of NH_3 and NO_2^- for $CuCoO_x$ after one-hour electrolysis in 0.1 M KOH with 1, 10, and 100 mM NO_3^- at different potentials. (**b**) Plots of the ammonia yield rate (Y_{NH3}) against the NO_3^- concentrations ($[NO_3^-]$) at -0.2 V, -0.1 V, and 0 V (vs. RHE).

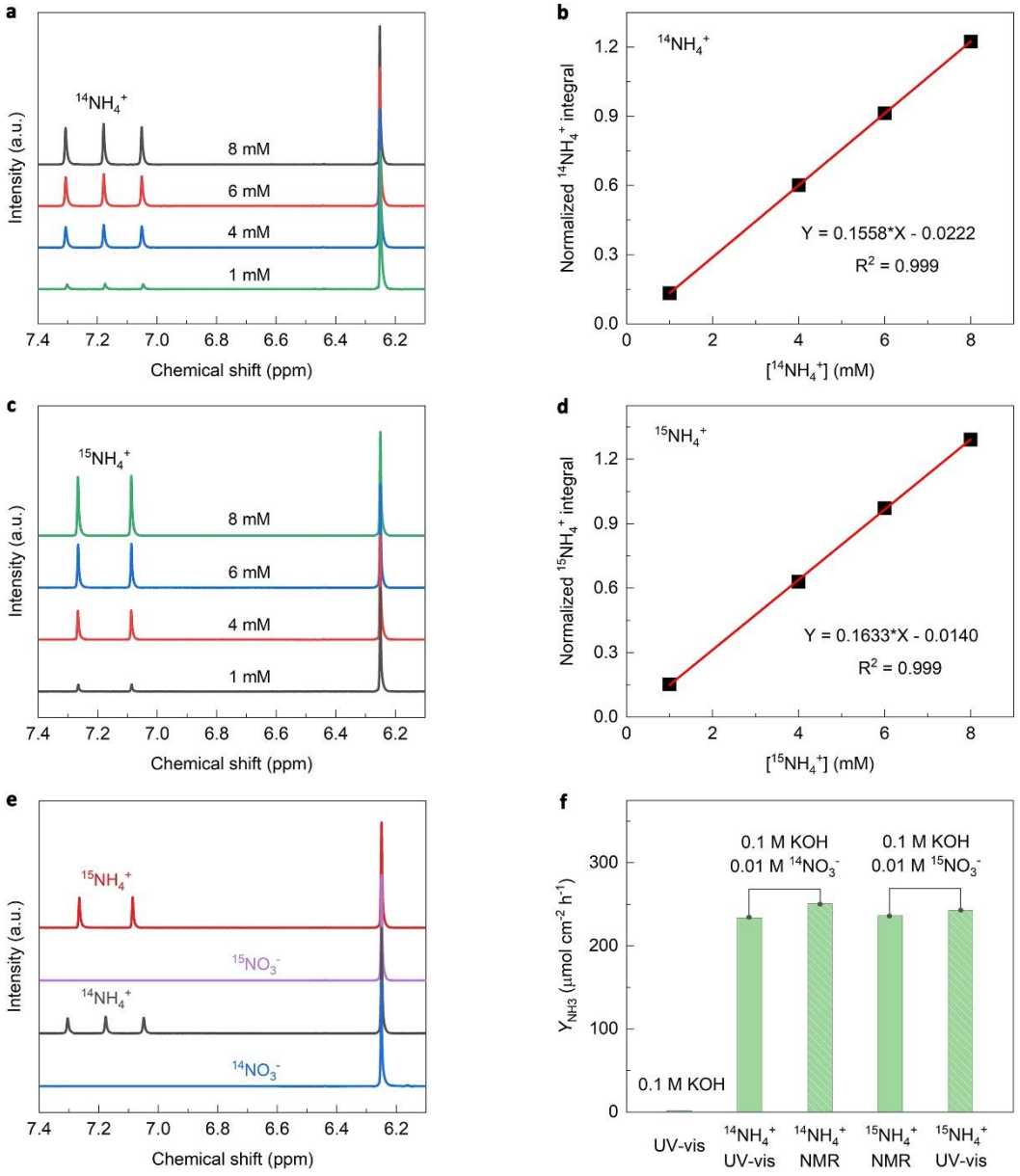

Figure S20. $^{14}NH_4^+$ and $^{15}NH_4^+$ quantification by ^{1}H NMR spectra. (**a**) ^{1}H NMR spectra of $^{14}NH_4^+$ ions with different concentrations. Maleic acid with a constant concentration was used as an external standard with a proton signal at δ = 6.25 ppm. (**b**) Calibration curve for $^{14}NH_4^+$ detection using ^{1}H NMR, where $^{14}NH_4^+$ peak area integrals were normalized to that of maleic acid. The normalized peak area integral of $^{14}NH_4^+$ is positively correlated to the concentrations of $^{14}NH_4^+$ [$^{14}NH_4^+$]. (**c**) ^{1}H NMR spectra of $^{15}NH_4^+$ ions with different concentrations. (**d**) Calibration curve for $^{15}NH_4^+$ detection using ^{1}H NMR, where $^{15}NH_4^+$ peak area integrals were normalized to that of maleic acid. (**e**) ^{1}H NMR spectra of the electrolytes after electrocatalysis using 0.01 M $^{15}NO_3^-$ or 0.01 M $^{14}NO_3^-$ in 0.1 M KOH as nitrogen source. ^{1}H NMR of the fresh electrolytes without going through electrolysis (marked as $^{15}NO_3^-$ and $^{14}NO_3^-$) were provided as controls, showing no background signals of ammonia. (**f**) Comparison of the ammonia yield rate over $CuCoO_x$ quantified by the UV−Vis spectra and ^{1}H NMR. The electrolysis was carried out at −0.1 V (*vs.* RHE) for one hour in 0.1 M KOH with and without 0.01 M $^{14}NO_3^-$ or 0.01 M $^{15}NO_3^-$.

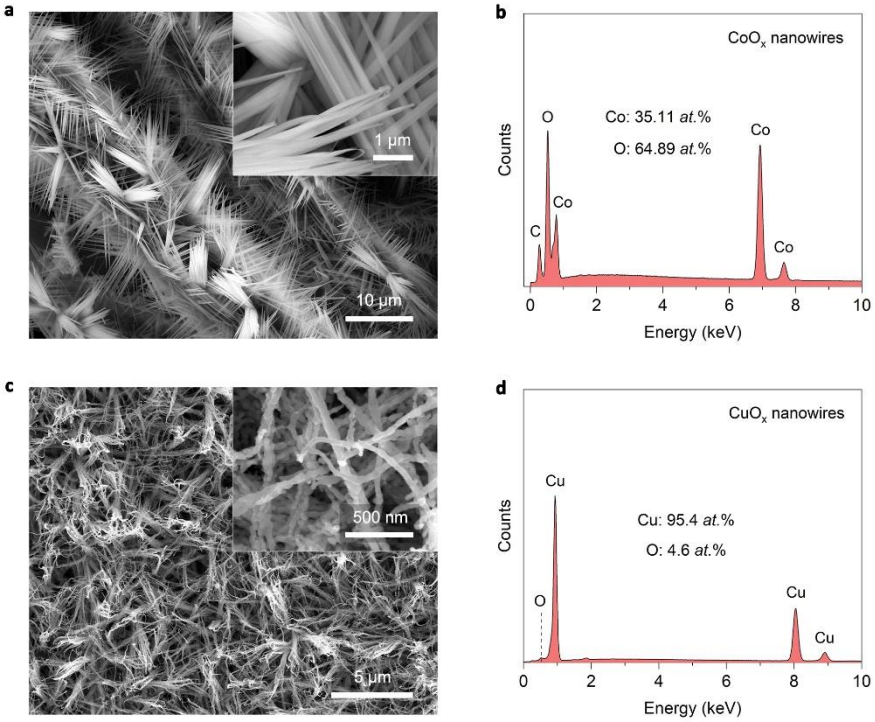

Figure S21. Morphology and composition of CoO_x and CuO_x nanowires. (**a**) SEM images of CoO_x nanowires on carbon paper with different magnifications. (**b**) The corresponding EDS spectra of CoO_x nanowires. (**c**) SEM images of CuO_x nanowires on Cu foil with different magnifications. (**d**) The corresponding EDS spectra of CuO_x nanowires.

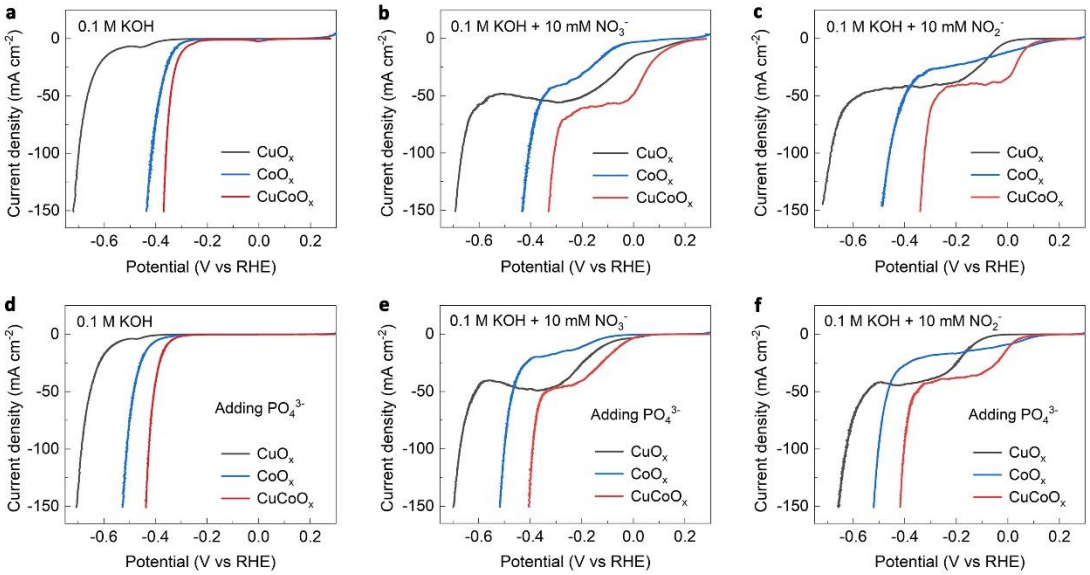

Figure S22. **The impact of adding PO_4^{3-} ions on the LSVs of CuO_x, CoO_x, and $CuCoO_x$ in 0.1 M KOH with and without 0.01 M NO_3^- or NO_2^-.** (**a-c**) Typical LSVs of the catalysts in 0.1 M KOH (**a**), 0.1 M KOH + 0.01 M NO_3^- (**b**), and 0.1 M KOH + 0.01 M NO_2^- (**c**). (**d-f**) With adding 0.1 M PO_4^{3-} (0.1 M Na_3PO_4), the corresponding LSVs of the catalysts in 0.1 M KOH (**d**), 0.1 M KOH + 0.01 M NO_3^- (**e**), and 0.1 M KOH + 0.01 M NO_2^- (**f**). Note that the addition of 0.1 M Na_3PO_4 shows an ignorable impact on the

pH values of the electrolytes (changing from 13.0 to ~13.04). The LSVs were recorded at a scan rate of 5 mV s^{-1}.

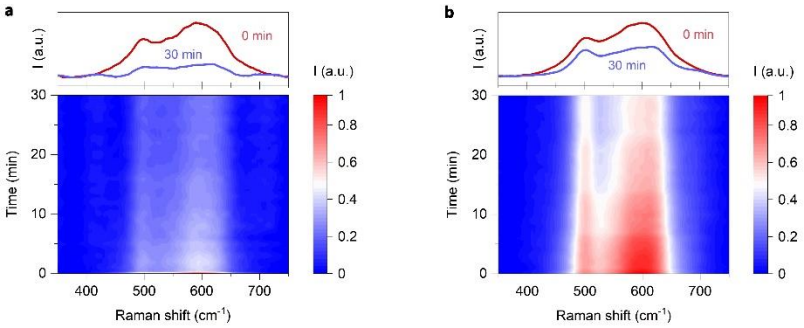

Figure S23. **Phase evolution of $CuCoO_x$_40mA and $CuCoO_x$_80mA with time under -0.1 V (vs. RHE).** Evolution of Raman spectra on $CuCoO_x$_40mA (**a**) and $CuCoO_x$_80mA (**b**) with time under the applied potential of -0.1 V (vs. RHE) in 0.1 M KOH (pH = 13). Typical Raman spectra of the samples at specific time points were given on the top of the figures.

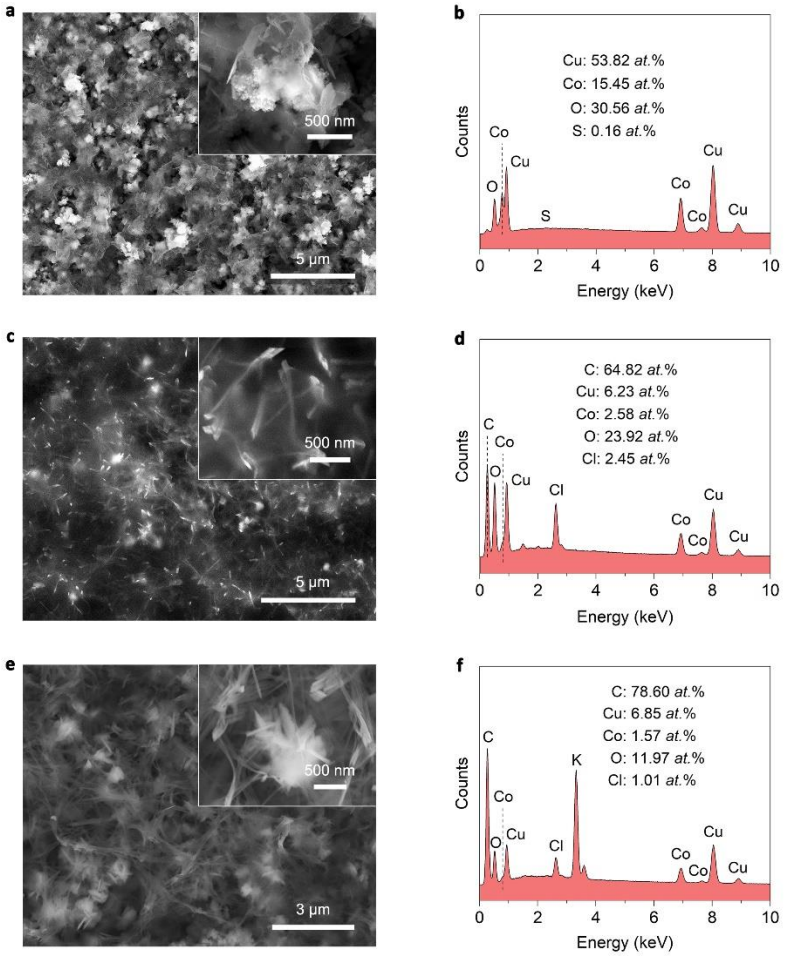

Figure S24. Morphology and composition of $CuCoO_x$ and CuCoOx_VRP after electrolysis in 0.1 M NO_3^-. (**a**) SEM images of $CuCoO_x$ nanoribbons after electrolysis in 0.1 M NO_3^- with different magnification. (**b**) The corresponding EDS spectra of $CoCoO_x$ after electrolysis. (**c**) SEM images of

$CuCoO_x$_VRP ($CuCoO_x$ nanoribbons coated by a layer of 0.1 mg cm^{-2} viologen-based redox polymers (VRP)). (**d**) The corresponding EDS spectra of $CuCoO_x$_VRP. (**e**) SEM images of $CuCoO_x$_VRP after electrolysis in 0.1 M NO_3^- with different magnification. (**f**) The corresponding EDS spectra of $CoCoO_x$_VRP after electrolysis.

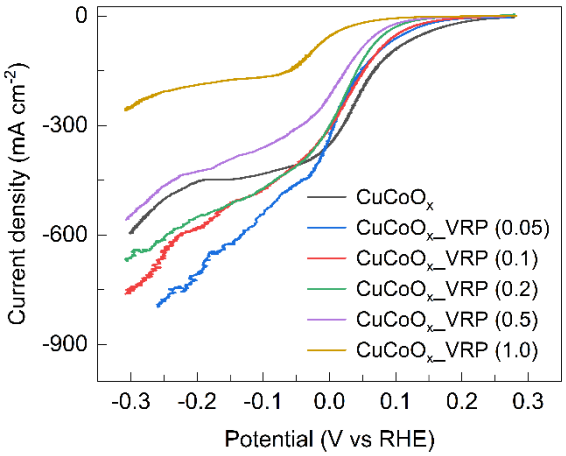

Figure S25. LSVs curves of $CuCoO_x$_VRP. The loading amounts of viologen-based redox polymers (VRP) on $CuCoO_x$ were adjusted from 0.05, 0.1, 0.2, 0.5 to 1.0 mg cm^{-2}. The LSV curves were recorded in 0.1 M KOH + 0.1 M NO_3^-. LSVs curves were recorded at a scan rate of 5 mV s^{-1}.

As shown in Figure S25, with a comparatively low mass loading (0.05-0.2 mg cm^{-2}) of the VRP, the $CuCoO_x$_VRP showed an increased transport-limited current density, suggesting that the positively charged VRP hydrogels can promote mass transfer of NO_3^- ions. As such, the slight increase in the NO_3RR overpotentials could be attributed to a possible reduction of NO_2 to NO_2^- on the VRP hydrogel layer, rather than on the $CuCoO_x$ catalyst, which led to a lower current on $CuCoO_x$_VRP at low applied potentials compared to the $CuCoO_x$. However, when the mass loading of VRP hydrogels was increased to 0.5 or 1 mg cm^{-2}, the potentials of $CuCoO_x$_VRP for the NO_3RR showed a drastic negative shift, accompanied by a sharply decreased transport-limited current density. These results suggest that the mass transport of NO_3^- ions is substantially limited by a thick VRP hydrogel layer (0.5 or 1 mg cm^{-2}). Considering the balance between the activity and stability of $CuCoO_x$_VRP, the optimal mass loading of the VRP was chosen to be 0.1 mg cm^{-2}.

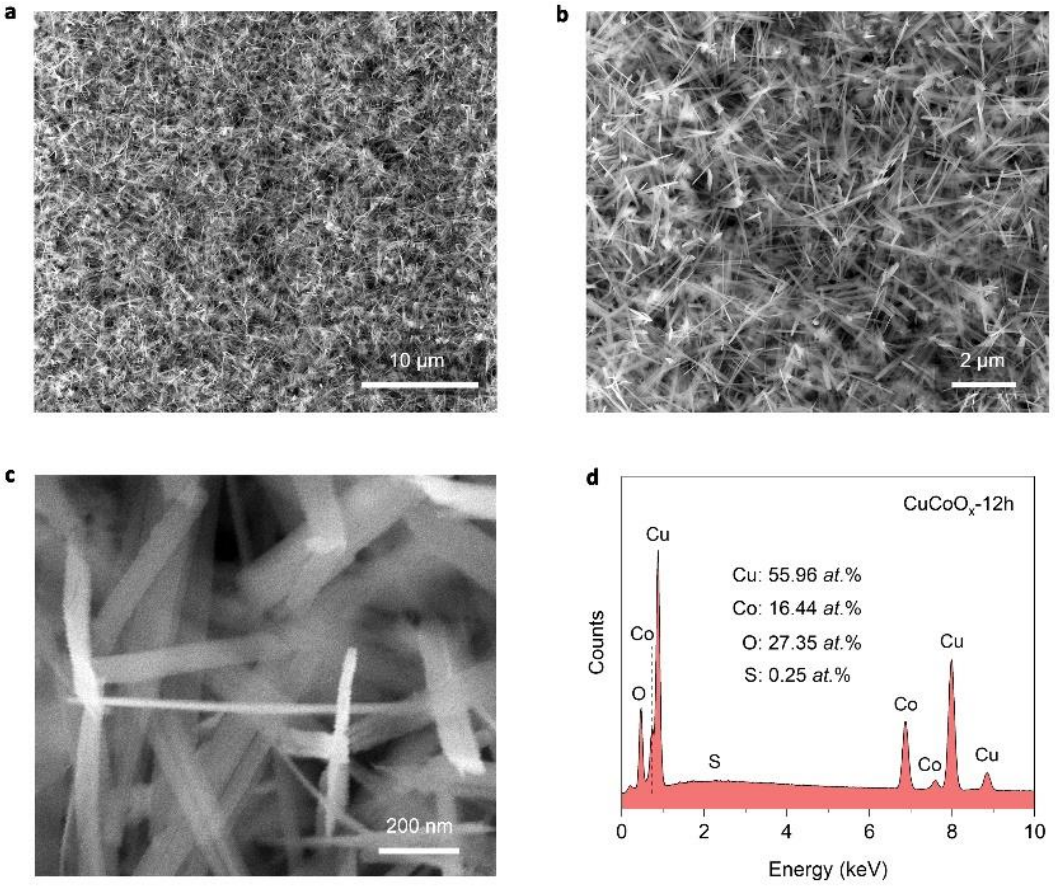

Figure S26. Morphology and composition of $CuCoO_x$ after 12 hours electrolysis (CuCoOx_12h) at -0.1 V (vs RHE) in 0.1 M KOH. (**a**−**c**) Typical SEM images of $CuCoO_x$_12h on Cu foil with different magnification. (**d**) EDS spectra of $CuCoO_x$_12h.

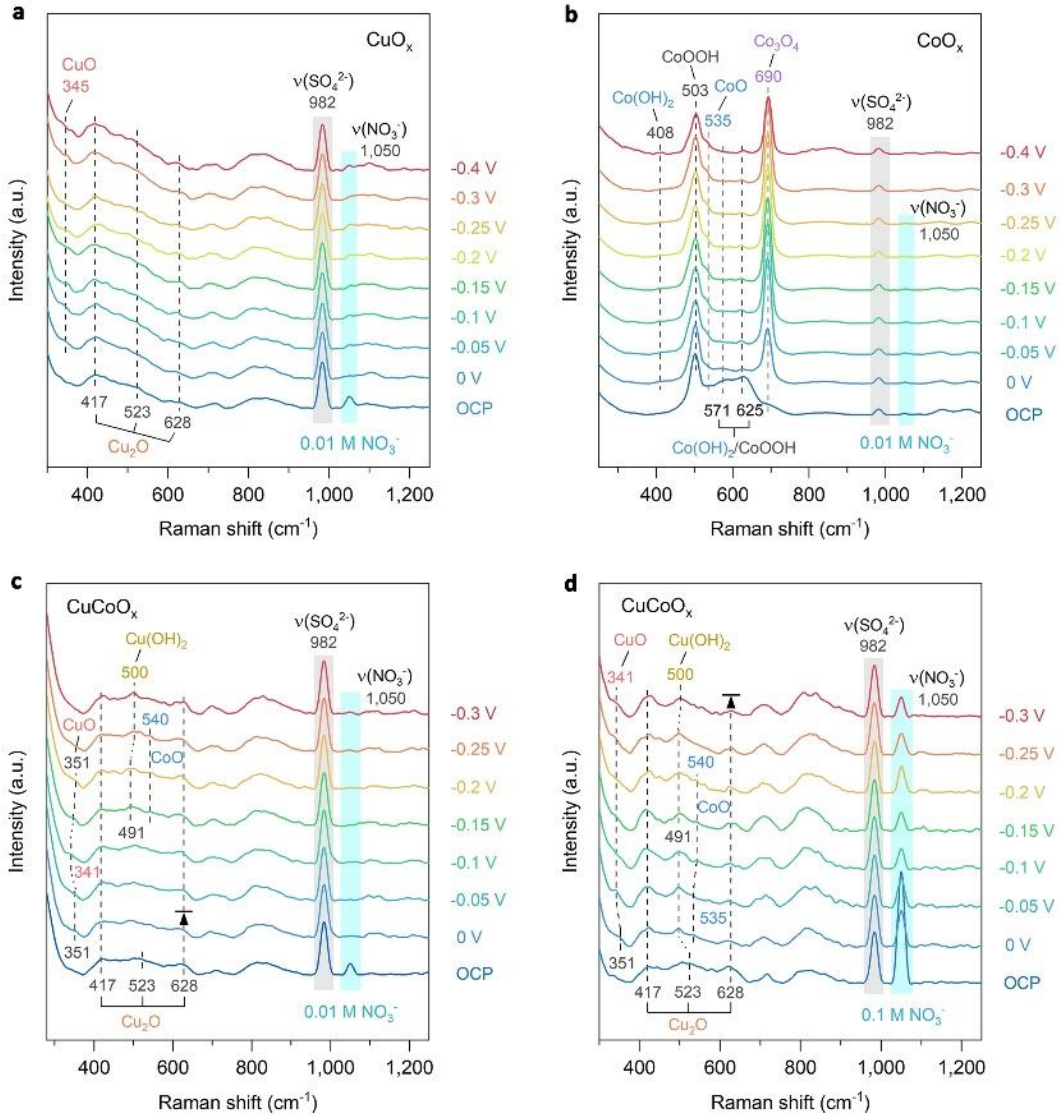

Figure S27. In−situ Raman spectra of the catalysts at a series of applied potentials. (**a**) CuO_x nanowires on Cu foil tested in 0.01 M KOH, 0.4 M K_2SO_4, and 0.01 M NO_3^-. (**b**) CoO_x nanowires on carbon paper tested in 0.01 M KOH, 0.4 M K_2SO_4, and 0.01 M NO_3^-. (**c**) $CuCoO_x$ nanoribbons on Cu foil tested in 0.01 M KOH, 0.4 M K_2SO_4, and 0.01 M NO_3^-. (**d**) $CuCoO_x$ nanoribbons on Cu foil tested in 0.01 M KOH, 0.4 M K_2SO_4, and 0.1 M NO_3^-. The Raman spectra were recorded after applying a constant potential for 10 min.

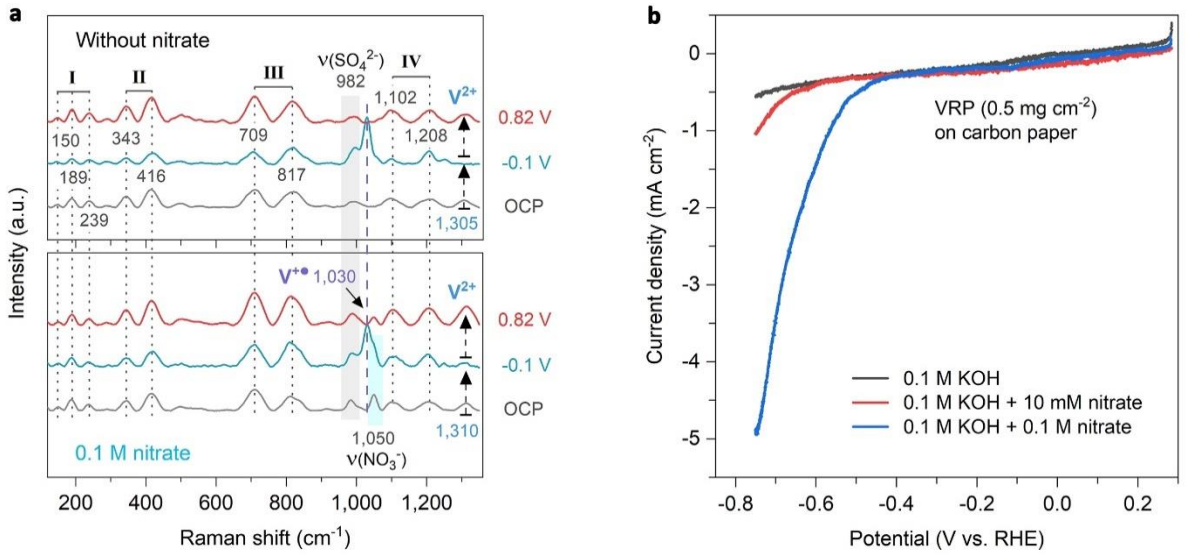

Figure S28. **In−situ Raman spectra and LSVs curves of viologen-based redox polymers (VRP) with and without 0.1 M NO_3^-.** (**a**) VRP (0.5 mg cm^{-2}) on carbon papers tested in 0.01 M KOH and 0.45 M K_2SO_4 without nitrate (up) and with 0.1 M NO_3^- (down). The Raman spectra were recorded after applying open-circuit potential (OCP) or a constant potential (vs. RHE) for 20 min. (**b**) LSV curves of VRP (0.5 mg cm^{-2}) on carbon paper in 0.1 M KOH, 0.1 M KOH + 0.01 M NO_3^-, and 0.1 M KOH + 0.1 M NO_3^-. LSVs were recorded at a scan rate of 5 mV s^{-1}.

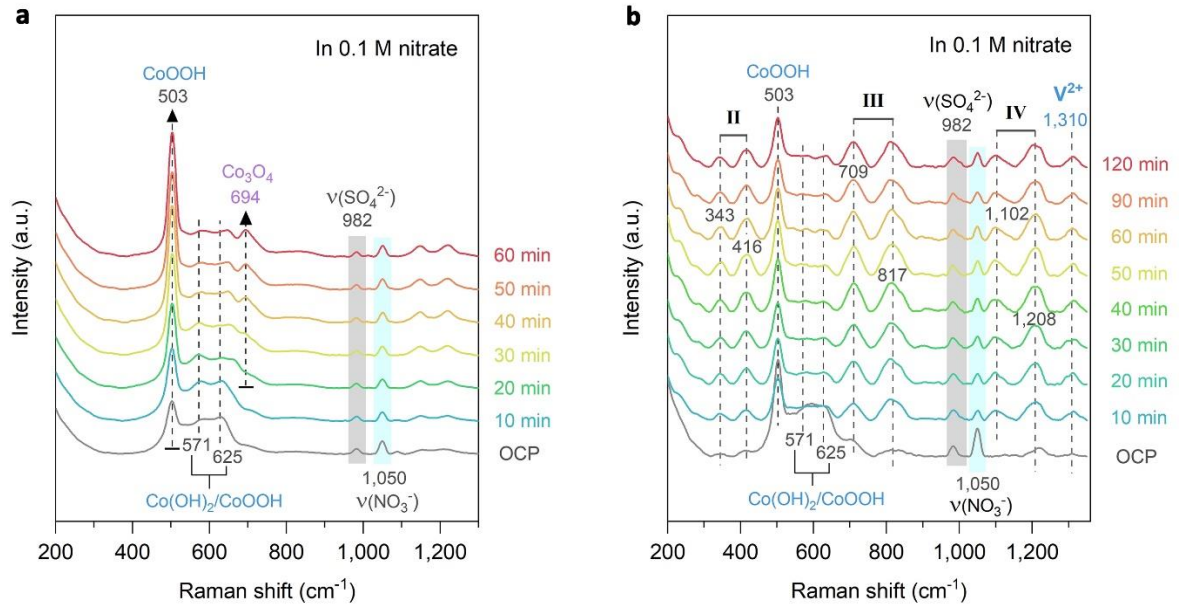

Figure S29. Phase evolution of CoO_x nanowires with and without a VRP coating layer under -0.1 V (vs. RHE). (**a**) CoO_x nanowires on carbon papers tested in 0.01 M KOH, 0.04 M K_2SO_4, and 0.1 M NO_3^-. (**b**) CoO_x nanowires with a VRP coating layer (0.5 mg cm^{-2}) on carbon papers tested in 0.01 M KOH, 0.04 M K_2SO_4, and 0.1 M NO_3^-.

Supplementary Tables

Table S1. Comparison of the NH_3 synthesis activity of $CuCoO_x$ catalyst with other catalysts reported to date using low-concentration nitrate (1-10 mM) as the nitrogen source under ambient conditions. Error denotes the standard deviations of yield rate and Faradaic efficiency calculation from three independent samples. This table shows the performance parameters of the catalysts at the highest Faradaic efficiency.

Catalysts	Electrolyte	The applied potential (V vs. RHE)	The highest FE (%)	NH_3 yield rate and geometric *j*	Half-cell EE_{NH3} (%)	E_c (kWh kg^{-1}_{NH3}) *	Reference
$CuCoO_x$ NRs *on Cu foil*	0.1 M KOH + 1 mM NO_3^-	-0.1	93.8 ±2.4	28.7 ±12.5 μmol h^{-1} cm^{-2} -4.7 mA cm^{-2}	38.7 ±1.0	-17.9 ±0.5	**This work**
	0.1 M KOH + 10 mM NO_3^-	-0.1	97.8 ±1.3	227.0 ± 14.5 μmol h^{-1} cm^{-2} -50.0 mA cm^{-2}	39.8 ±0.5	-17.2 ±0.2	
CuNi alloy *on PTFE film*	1 M KOH + 1 mM NO_3^-	-0.17	65 ± 3	-1.2 mA cm^{-2}	25.82	-27.2	Edward H. Sargent et al.[10]
	1 M KOH + 10 mM NO_3^-	-0.15	93 ± 2	-6.5 mA cm^{-2}	37.0	-18.7	
CuCoSP *on Cu foil*	0.1 M KOH + 1 mM NO_3^-	-0.175	91.2	15.7 μmol h^{-1} cm^{-2} -3.5 mA cm^{-2}	35.6	-19.4	W. Schuhmann et al.[11]
	0.1 M KOH + 10 mM NO_3^-	-0.175	92.8 ± 1.7	151.6 μmol h^{-1} cm^{-2} -35.7 mA cm^{-2}	35.8	-19.1	
OD-Cu *on Cu foam*	1 M KOH + 1 mM NO_3^-	-0.15	55.1	14 μmol h^{-1} cm^{-2}	22.2	-31.6	Y. Tang and C. Liu et al.[12]
Cu@C *on carbon paper*	1 M KOH + 1 mM NO_3^-	-0.3	72	J_{NH3} = ~-3.8 mA cm^{-2}	26.2	-26.8	Z. Geng et al.[13]
CuCl_BEF *on carbon cloth*	0.5 M Na_2SO_4 + 100 mg L^{-1} NO_3^- (~7.1 mM)	-1.0	44.7	107.1 μmol h^{-1} cm^{-2}	10.0	-62.9	J. Lu et al.[14]
Ni_{35}/NC-sd *on Titanium mech*	0.5 M Na_2SO_4 + 5 mM NO_3^-	-0.5	96	22.4 μmol h^{-1} cm^{-2}	27.7	-22.7	X. Li et al.[15]
Ni_3B@$NiB_{2.74}$ *on carbon paper*	0.1 M KOH + 1 mM NO_3^-	-0.4	90.7	~17.04 μmol h^{-1} cm^{-2}	30.5	-22.7	S. Qiao et.al.[16]
	0.1 M KOH + 10 mM NO_3^-	-0.4	98.7	107.1 μmol h^{-1} cm^{-2}	32.8	-20.8	
Strained Ru nanoclusters *on carbon paper*	1 M KOH + 1 mM NO_3^-	-0.2	90	~-3.6 mA cm^{-2}	35.0	-20.0	L. Zhang et al.[17]

***Energy consumption**: The energy consumption (E_C, kWh kg_{NH3}^{-1}) for electrocatalytic NO_3^--to-ammonia conversion was obtained assuming the overpotential of the water oxidation at anode is zero. $E_C(NH_3) = n \times F \times (1.23 - E)/(3600 \times m \times FE)$, where n is the electron number for producing ammonia (n = 8 for

NO_3RR); E is the applied potential (vs. RHE) for NH_3 production; m is the mole mass of NH_3 (17 g mol^{-1}); FE is the Faradaic efficiency.

Table S2. Comparison of the NH_3 synthesis activity of $CuCoO_x$ catalyst with other catalysts reported to date using high-concentration nitrate (14.3 mM to 1 M) as the nitrogen source under ambient conditions. Error denotes the standard deviations of NH_3 yield rate and Faradaic efficiency (FE) calculation from three independent samples. This table shows the performance parameters of the catalysts at the highest Faradaic efficiency.

Catalysts	Electrolyte	The applied potential (V vs. RHE)	The highest FE (%)	NH_3 yield rate and Geometric *j*	Half-cell EE_{NH3} (%)	E_c (kWh kg_{NH3}^{-1})*	Reference
$CuCoO_x$ NRs *on Cu foil*	0.1 M KOH + 0.1 M NO_3^-	0	94.9 ±2.5	0.87 ±0.18 mmol h^{-1} cm^{-2}	41.9 ±0.25	-16.4 ±0.4	**This work**
		-0.1	97.7 ±1.0	1.95 ±0.2 mmol h^{-1} cm^{-2} -415.4 mA cm^{-2}	39.3 ±0.4	-17.2 ±0.2	
CuCoSP on *Cu foil*	0.1 M KOH + 0.1 M NO_3^-	-0.175	90.6	1.17 mmol h^{-1} cm^{-2} -279.1 mA cm^{-2}	34.4	-19.6	W. Schuhmann et. al[11]
CuNi alloy *on Cu foam*	1 M KOH + 0.1 M NO_3^-	-0.1	~95	-90 mA cm^{-2}	37.6	-17.7	Edward H. Sargent et al.[10]
$FeCo_2O_4$ nanowires *on carbon cloth*	0.1 M KOH + 20 mM NO_3^-	-0.5	95.9	293.4 µmol h^{-1} cm^{-2}	29.8	-22.8	X. Sun et. al[18]
$CuO@MnO_2$ /CF *on Cu foam*	0.5 M K_2SO_4 +200 ppm NO_3^--N (~14.3 mM)	-1.3 V *vs.* SCE (-0.64 V *vs.* RHE)	94.9	240 µmol h^{-1} cm^{-2}	25.2	-24.9	L. Wang, H, Wang et. al[19]
Co/TiO_2 NSs *on carbon cloth*	1 M PBS + 0.4 M NO_3^-	-0.72	97.4	223 µmol h^{-1} cm^{-2}	24.2	-25.3	Y. Cao et. al[20]
$Cu_{0.5}Co_{0.5}$ alloy *on carbon paper*	1 M KOH + 50 mM NO_3^-	-0.03	95	-177 mA cm_{-2}	41.0	-16.7	H. Wang et. al[21]
CuPd nanocubes *on carbon paper*	1 M KOH + 1 M NO_3^-	-0.6	92.5	1.25 mmol h^{-1} cm^{-2}	27.0	-25.0	H. Xin and H. Zhu et. al[22]
Cu/Cu_2O NWAs *on Cu mesh*	0.5 M Na_2SO_4 + 200 ppm NO_3^- (~14.3 mM)	-0.85	81	0.2449 mmol h^{-1} cm^{-2}	19.3	-32.4	B. Zhang et al.[23]
OD-Cu *on Cu foam*	1 M KOH + 0.1 M NO_3^-	-0.2	92	1.1 mmol h^{-1} cm^{-2}	33.9	-19.6	Y. Tang and C. Liu et al.[12]
Cu@C *on carbon paper*	1 M KOH + 0.1 M NO_3^-	-0.7	99.3	~1.0 mmol h^{-1} cm^{-2}	27.1	-24.5	Z. Geng et al.[13]
Co/CoO NSAS *on Ni foam*	0.1 M Na_2SO_4 + 200 ppm NO_3^--N (~14.3 mM)	-1.3 V *vs.* SCE (-0.64 V *vs.* RHE)	~93.8	194.46 µmol h^{-1} cm^{-2}	24.9	-25.1	B Zhang et al.[24]
CoP NSs *on carbon cloth*	1 M KOH + 1 M NO_3^-	-0.3	~100	0.956 mmol h^{-1} cm^{-2}	34.9	-19.3	J. Liu et al.[25]

Ni_3B@$NiB_{2.74}$ *on carbon paper*	0.1 M KOH + 0.1 M NO_3^-	-0.2	100	198.3 μmol h^{-1} cm^{-2}	37.3	-18.0	S. Qiao et al.[16]
Ni_{35}/NC-sd *on Titanium mesh*	0.5 M Na_2SO_4 + 0.3 M NO_3	-0.5	99	70.6 μmol h^{-1} cm^{-2}	27.8	-22.0	X. Li et al.[15]
PTCDA/O-Cu *on carbon cloth*	0.1 M PBS and 500 ppm NO_3^--N (35.7 mM)	-0.4	77 ± 3	436 ± 85 μg h^{-1} cm^{-2}	23.3	-26.7	H. Wang et al.[26]
Cu@Th-BPYDC *on carbon paper*	1 M KOH and 0.1 M NO_3^-	0	92.5	225.3 μmol h^{-1} cm^{-2}	39.6	-16.8	F. Luo et al.[27]
Fe-ppy SACs *on carbon paper*	0.1 M KOH + 0.1 M NO_3^-	-0.5	~100	73 μmol h^{-1} cm^{-2}	30.9	-21.8	G. Yu et al.[28]
Cu-N-C SAC *on carbon paper*	0.1 M KOH + 0.1 M NO_3^-	-1.0	84.7	264.7μmol h^{-1} cm^{-2}	20.3	-33.2	A. Wang et al.[29]
Strained Ru NCs *on carbon paper*	1 M KOH and 1 M NO_3^-	-0.2	~100	1.17 mmol h^{-1} cm^{-2} -128.1 mA cm^{-2}	37.3	-18.0	L. Zhang et al.[17]
a-RuO_2 on *carbon paper*	0.5 M Na_2SO4 + 200 ppm NO_3^--N (~14.3 mM)	-0.35	97.46	115.8 μmol h^{-1} cm^{-2}	30.6	-20.4	Y. Yu et al.[30]

***Energy consumption**: The energy consumption (E_C, kWh kg_{NH3}^{-1}) for electrocatalytic NO_3^--to-ammonia conversion was obtained assuming the overpotential of the water oxidation at anode is zero. $E_C(NH_3) = n \times F \times (1.23 - E)/(3600 \times m \times FE)$, where n is the electron number for producing ammonia (n = 8 for NO_3RR); E is the applied potential (vs. RHE) for NH_3 production; m is the mole mass of NH_3 (17 g mol^{-1}); FE is the Faradaic efficiency.

Table S3. Electrochemical double−layer capacitance derived ECSA. The ECSA of a smooth Cu foil is defined to be 1 cm^2. The ECSA of the other samples is determined by: ECSA = C_{dl}/C_0, where C_0 is double layer capacitance per geometric electrode area of a smooth Cu foil, and C_{dl} is the double layer capacitance per geometric electrode area of the samples. In this study, the C_0 = 0.126 mF cm^{-2} was used according to our previous study,[11] while the C_{dl} was obtained from the slopes in **Figure S12f**.

Electrode	Capacitance per electrode area C_{dl} (mF cm^{-2})	ECSA (cm^2)
Cu foil	0.126	1.0
$CuCoO_x$	2.47	19.6
$CuCoO_x$_40mA	2.80	22.2
$CuCoO_x$_80mA	2.61	20.7
CuO_x nanowires	3.15	25.0

CoO_x nanowires	4.52	35.9

References

[1] a) W. He, R. Ifraemov, A. Raslin, I. Hod, *Adv. Funct. Mater.* **2018**, *28*, 1707244; b) W. He, I. Liberman, I. Rozenberg, R. Ifraemov, I. Hod, *Angew. Chem. Int. Ed.* **2020**, *59*, 8262-8269.

[2] J. Tian, Q. Liu, A. M. Asiri, X. Sun, *J. Am. Chem. Soc.* **2014**, *136*, 7587-7590.

[3] a) G. Kresse, J. Furthmüller, *Comp. Mater. Sci.* **1996**, *6*, 15-50; b) G. Kresse, J. Furthmüller, *Phy. Rev. B* **1996**, *54*, 11169-11186.

[4] J. P. Perdew, K. Burke, M. Ernzerhof, *Phys. Rev. Lett.* **1996**, *77*, 3865-3868.

[5] P. E. Blöchl, *Phy. Rev. B* **1994**, *50*, 17953-17979.

[6] L. Wang, T. Maxisch, G. Ceder, *Phys. Rev. B* **2006**, *73*, 195107.

[7] L. Chen, C. Tang, K. Davey, Y. Zheng, Y. Jiao, S.-Z. Qiao, *Chem. Sci.* **2021**, *12*, 8079-8087.

[8] M. Passon, A. Ruff, P. Schuler, B. Speiser, W. Leis, *J. Solid State Electrochem.* **2015**, *19*, 85-101.

[9] L. H. Eng, M. Elmgren, P. Komlos, M. Nordling, S.-E. Lindquist, H. Y. Neujahr, *J. Phys. Chem.* **1994**, *98*, 7068-7072.

[10] Y. Wang, A. Xu, Z. Wang, L. Huang, J. Li, F. Li, J. Wicks, M. Luo, D.-H. Nam, C.-S. Tan, Y. Ding, J. Wu, Y. Lum, C.-T. Dinh, D. Sinton, G. Zheng, E. H. Sargent, *J. Am. Chem. Soc.* **2020**, *142*, 5702-5708.

[11] W. He, J. Zhang, S. Dieckhöfer, S. Varhade, A. C. Brix, A. Lielpetere, S. Seisel, J. R. C. Junqueira, W. Schuhmann, *Nat. Commun.* **2022**, *13*, 1129.

[12] J. Yuan, Z. Xing, Y. Tang, C. Liu, *ACS Appl. Mater. Interfaces* **2021**, *13*, 52469-52478.

[13] Z. Song, Y. Liu, Y. Zhong, Q. Guo, J. Zeng, Z. Geng, *Adv. Mater.* **2022**, *34*, 2204306.

[14] W.-J. Sun, H.-Q. Ji, L.-X. Li, H.-Y. Zhang, Z.-K. Wang, J.-H. He, J.-M. Lu, *Angew. Chem. Int. Ed.* **2021**, *60*, 22933-22939.

[15] P. Gao, Z.-H. Xue, S.-N. Zhang, D. Xu, G.-Y. Zhai, Q.-Y. Li, J.-S. Chen, X.-H. Li, *Angew. Chem. Int. Ed.* **2021**, *60*, 20711-20716.

[16] L. Li, C. Tang, X. Cui, Y. Zheng, X. Wang, H. Xu, S. Zhang, T. Shao, K. Davey, S.-Z. Qiao, *Angew. Chem. Int. Ed.* **2021**, *60*, 14131-14137.

[17] J. Li, G. Zhan, J. Yang, F. Quan, C. Mao, Y. Liu, B. Wang, F. Lei, L. Li, A. W. M. Chan, L. Xu, Y. Shi, Y. Du, W. Hao, P. K. Wong, J. Wang, S.-X. Dou, L. Zhang, J. C. Yu, *J. Am. Chem. Soc.* **2020**, *142*, 7036-7046.

[18] J. Li, D. Zhao, L. Zhang, L. Yue, Y. Luo, Q. Liu, N. Li, A. A. Alshehri, M. S. Hamdy, Q. Li, X. Sun, *Chem. Commun.* **2022**, *58*, 4480-4483.

[19] Y. Xu, Y. Sheng, M. Wang, T. Ren, K. Shi, Z. Wang, X. Li, L. Wang, H. Wang, *J. Mater. Chem. A* **2022**, *10*, 16883-16890.

[20] Y.-T. Xu, Y. Han, D. K. Sam, Y. Cao, *J. Mater. Chem. A* **2022**, *10*, 22390-22398.

[21] T. H. Jeon, Z.-Y. Wu, F.-Y. Chen, W. Choi, P. J. J. Alvarez, H. Wang, *J. Phys. Chem. C* **2022**, *126*, 6982-6989.

[22] Q. Gao, H. S. Pillai, Y. Huang, S. Liu, Q. Mu, X. Han, Z. Yan, H. Zhou, Q. He, H. Xin, H. Zhu, *Nat. Commun.* **2022**, *13*, 2338.

[23] Y. Wang, W. Zhou, R. Jia, Y. Yu, B. Zhang, *Angew. Chem. Int. Ed.* **2020**, *59*, 5350-5354.

[24] Y. Yu, C. Wang, Y. Yu, Y. Wang, B. Zhang, *Sci. China Chem.* **2020**, *63*, 1469-1476.

[25] S. Ye, Z. Chen, G. Zhang, W. Chen, C. Peng, X. Yang, L. Zheng, Y. Li, X. Ren, H. Cao, D. Xue, J. Qiu, Q. Zhang, J. Liu, *Energy Environ. Sci.* **2022**, *15*, 760-770.

[26] G.-F. Chen, Y. Yuan, H. Jiang, S.-Y. Ren, L.-X. Ding, L. Ma, T. Wu, J. Lu, H. Wang, *Nat. Energy* **2020**, *5*, 605-613.

[27] Z. Gao, Y. Lai, Y. Tao, L. Xiao, L. Zhang, F. Luo, *ACS Central Science* **2021**, *7*, 1066-1072.

[28] P. Li, Z. Jin, Z. Fang, G. Yu, *Energy Environ. Sci.* **2021**, *14*, 3522-3531.

[29] J. Yang, H. Qi, A. Li, X. Liu, X. Yang, S. Zhang, Q. Zhao, Q. Jiang, Y. Su, L. Zhang, J.-F. Li, Z.-Q. Tian, W. Liu, A. Wang, T. Zhang, *J. Am. Chem. Soc.* **2022**, *144*, 12062-12071.

[30] Y. Wang, H. Li, W. Zhou, X. Zhang, B. Zhang, Y. Yu, *Angew. Chem. Int. Ed.* **2022**, *61*, e202202604.